COMPUTER AIDED DIAGNOSTIC SYSTEM FOR BRAIN TUMOR CLASSIFICATION

A Dissertation submitted in fulfillment of the requirements for the Degree

of

MASTER OF ENGINEERING

in

Electronic Instrumentation & Control Engineering

Submitted by

PUNEET TIWARI
801351019

Under the Guidance of

Dr. JAINY SACHDEVA
ASSISTANT PROFESSOR, EIED

2015

Electrical and Instrumentation Engineering Department

Thapar University, Patiala

(Declared as Deemed-to-be-University u/s 3 of the UGC Act., 1956)

Post Bag No. 32, Patiala – 147004

Punjab (India)

DECLARATION

I hereby certify that the work which is presented in dissertation entitled, "Computer Aided Diagnostic System for Brain Tumor Classification", in partial fulfillment of the requirements for the award of the degree of Master of Engineering in Electronic Instrumentation & Control, submitted to Electrical & Instrumentation Engineering Department of Thapar University, Patiala is as authentic record of my own work carried under the supervision of Dr. Jainy Sachdeva. It refers others researcher's work which is duly listed in the reference section. The matter contained in this dissertation has not been submitted, neither in part nor in full to any other degree to any other university or institute except as reported in the text and references.

Puneet Tiwari

Puneet Tiwari

801351019

Place: Patiala

Date: 13/07/2015

It is certified that the above statement made by the student is correct to the best of my/our knowledge and belief.

Jainy Sachdeva 13/07/2015

Dr. Jainy Sachdeva

Electrical and Instrumentation Engineering Department
Thapar University, Patiala - 147004

Date: 13-07-2015

Countersigned by:

Dr. Ravinder Agarwal
Professor and Head
Electrical and Instrumentation Engineering Department
Thapar University
Patiala – 147004

Dr. S.S. Bhatia
Dean of Academic Affairs
Thapar University
Patiala –147004

Dedicated to

My parents

ACKNOWLEDGEMENT

Foremost of all, I would like to show my gratitude to **Dr. Jainy Sachdeva**, Assistant Professor, Electrical and Instrumentation Engineering Department, Thapar University, Patiala for her patient guidance and funding throughout this story. I am really very fortunate to receive the chance to play with her. I found this guide to be extremely valuable.

I am also thankful to our Head of Department, **Dr. R. Agarwal** as well as PG coordinator, **Mr. Nirbhowjap Singh**, Assistant professor, Electrical and Instrumentation Engineering Department. I would like to thank the entire faculty and staff of Electrical and Instrumentation Engineering Department and my friends who devoted their valuable time and help me in all possible ways towards successful completion of this work. I thank all those who have contributed directly or indirectly to this work.

Lastly, I would like to thank my parents for their years of unyielding love and encourage. They have always wanted the best for me and I admire their determination and sacrifice.

Puneet Tiwari

PUNEET TIWARI

TABLE OF CONTENTS

LIST OF FIGURES

LIST OF TABLES

LIST OF ABBREVIATIONS

Main symbols and notations used in this study are listed below. Sometimes a symbol may have alternate meaning but in such a case; the context is sufficient to avoid confusion.

ANN	Artificial neural network
AST	Astrocytoma brain tumor
CAD	Computer aided diagnosis
FOS	First order statistics
GLCM	Gray level co-occurrence matrix
GLO	Glioma brain tumor
GLRLM	Gray level run-length matrix
GWT	Gabor wavelet filters
LTEM	Law's textural energy features
METS	Metastatic brain tumor
MENI	Meningioma brain tumor
MRI	Magnetic resonance imaging
ROI	Region of interest
WHO	World health organization

ABSTRACT

The iso, hypo or hyper intensity, similarity of shape, size and location complicates the identification of brain tumors. Therefore, an adequate Computer Aided Diagnosis (CAD) system is designed for classification of brain tumor for assisting inexperience radiologists in diagnosis process. A multifarious database of real post contrast T1-weighted MR images from 10 patients has been taken. This database consists of primary brain tumors namely Meningioma (MENI- class 1), Astrocytoma (AST- class 2), and Normal brain regions (NORM- class 3). The Region of Interest(s) (ROIs) of size 20 x 20 is extracted by the radiologists from each image in the database. A total of 371 texture and intensity features are extracted from these ROI(s). An Artificial Neural Network (ANN) is used to classify these three classes as it shows better classification results on multivariate non-linear, complicated, rule based domains, and decision making domains. It is being observed that ANN provides much accurate results in terms of individual classification accuracy and overall classification accuracy. The two discrete experiments have been performed. Initially, the experiment was performed by extracting 263 features and an overall classification accuracy 78.10% is achieved, however it was noticed that MENI (class-1) was highly misclassified with AST (class-2). Further, to improve the overall classification accuracy and individual classification accuracy specifically for MENI (class-1), LAW's textural energy measures (LTEM) were added in the feature bank (263+108=371). The texture patterns obtained were clear enough to differentiate between MENI (class-1) and AST (class-2) despite of necrotic and cystic component and location and size of tumor. LTEM features detected fundamental texture properties such as level, edge, spot, wave and ripple in both horizontal and vertical directions which boosted the texture energy. An individual class accuracy of 91.40% is obtained for MENI (class-1), 91.43% for AST (class-2), 94.29% for NORM (class-3) and an overall classification accuracy of 92.43% is achieved.

Keywords: Computer aided diagnosis (CAD), Region of interest(s) (ROIs), Magnetic resonance (MR), Artificial neural network (ANN), Graphical user interface (GUI)

CHAPTER 1

INTRODUCTION

1.1 BRAIN

The human brain controls whole functionality of the body mainly movements of organs, secretion of organs etc. The most important central part of the body is the brain which is very sensitive, and complex. The interior of brain has sophisticated and subtle structure. Every interior cell of the brain is surrounded and connected together in a complex way. This part of

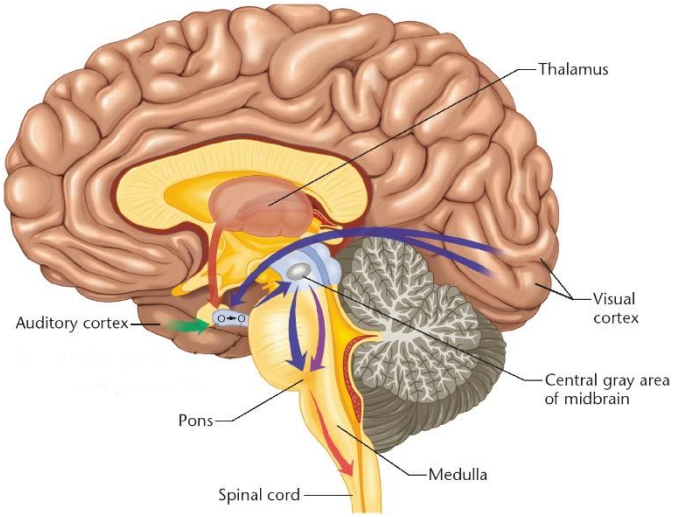

Fig. 1.1 Human brain[1]

human body is very sensitive so it can be affected by any damage and thus damages the entire body badly. It is surrounded by a protective skull which provides protection to the whole brain from damages. The development of aberrant cells in the body causes tumor. Despite being protective by the protective layer, a brain tumor can affect brain from inside which causes structural change and functionality of the brain.

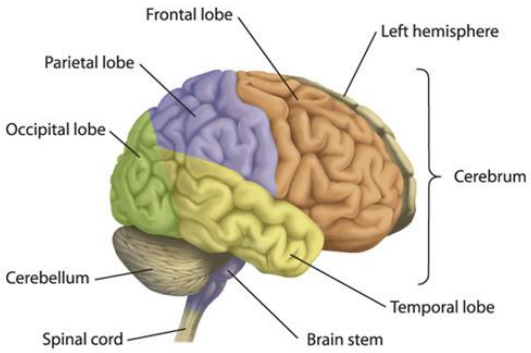

Fig. 1.2 Different parts of the human brain

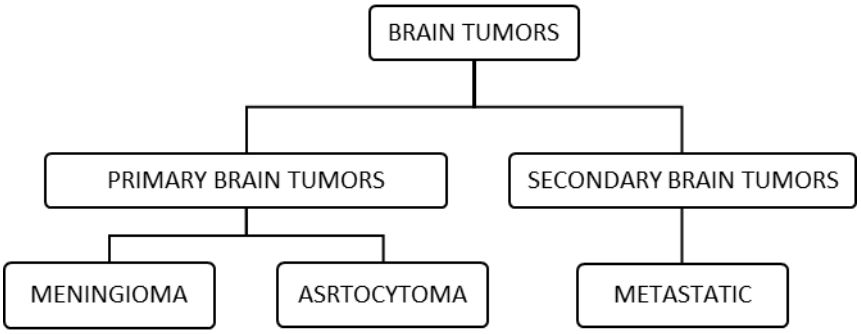

Fig. 1.3 Different types of brain tumor

Brain tumors are of the following types:

1.1.1 PRIMARY BRAIN TUMORS

Primary brain tumorsare of two types named as benign and malignant. Benign brain tumors are basically noncancerous with well-defined borders and usually are not intensely rotated within brain tissues by virtue of which it is surgically easy to remove primary brain tumors. After surgery primary brain tumor may grow again although there is less chances to reappear than malignant brain tumor. Benign brain tumors have a slow growth-rate and does not have a tendency to invade adjacent healthy tissues. Although with non-infiltrating nature benign is not dangerous but sometimes it may produce adverse health issues. The growth of the benign tumor produces a “mass effect” that can squeeze tissues and may cause tissue death (necrosis), damage in nerves, and blood flow reduction to a particular area of the body (Ischaemia). Benign brain tumor causes inflammation and increases pressure on adjacent healthy tissues as well as tissues inside the skull. Mostly benign tumors are not deadly but some can convert into a cancerous (malignant) tumour through a process named as “tumor progression”. This is the reason for which surgery is needed to remove benign tumor in order to prevent other adverse health issues. [1][2]

Second type of primary brain tumor is malignant brain tumors which are cancerous in nature. Malignant brain tumor has a different cell structure from normal brain cells just like benign brain tumor. The origin of these type of brain tumor is within the brain with a much higher growing rate. Malignant brain tumors has faster growth which invade surrounding tissues aggressively. These may retreat sometimes from primary cancer sites and have a tendency to spread to other locations. After shifting to other locations malignant brain tumors produce another tumour at that location. Primary brain tumors are rarely found beyond the brain or spinal area.

Any tumor that starts in the brain falls in primary brain tumor category. The origins of primary brain tumor are mainly brain cells, membrane around brain (meninges), nerves, or glands. The brain tumors produce inflammation, produce pressure on adjacent brain tissues, and place pressure within the skull. Till date the cause of primary brain tumor is unidentified but some possible factors which can play a role are as following:

a) Various radiation therapies are used to treat brain cancers which escalates the risk for brain tumors.
b) Cell phones are frequently debated as a risk for brain tumor. However, recent studies have obtained results according to which wireless devices, cell phones, and cordless devices do not increases the risk.
c) With a weak immune system, lymphomas starts to grow in the brain. This can be related to the Epstein-Barr virus (EBV). EBV and cytomegalovirus (CMV) are common virus that have been found in brain tumors.

Brain tumors can be categorised depending on:

a) Tumor location
b) Type of tissues involvement
c) Benign and malignant
d) Other factors also

1.1.1.1 MENINGIOMA BRAIN TUMOR (MENI)

Meningioma brain tumors often appear from the spinal cord and the brain covering. These tumors originated from the meninges. It is the three thin layers of cells which covers the spinal cord and the brain. The most common locations of MENI is the outer and top curve of the brain. These can be at the bottom of the brain skull. MENI has a tendency to grow

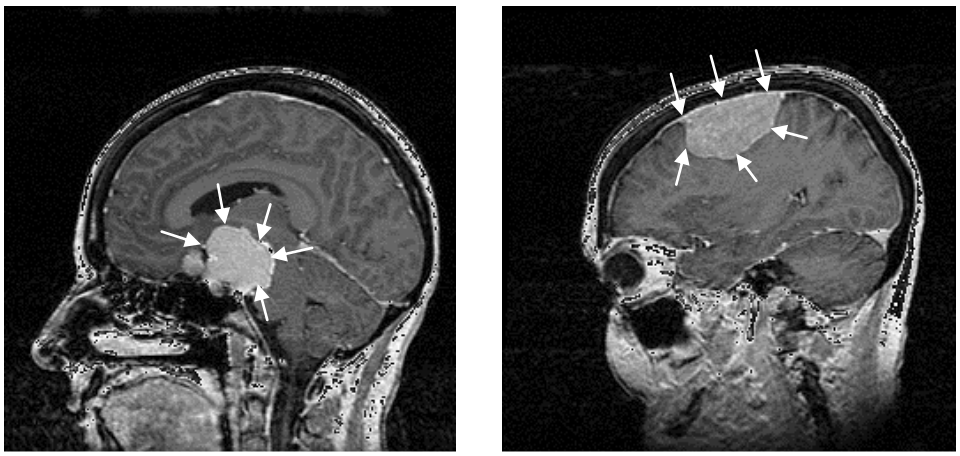

Fig. 1.4 Meningioma brain tumor with different locations

inward which causes an inside pressure on the spinal cord or the brain. These tumors can also expand towards the skull which causes the skull to thicken.

1.1.1.2 ASTROCYTOMA (AST)

The origin of mostly primary brain tumors is in glial cells while Astrocytoma has its origin in a special kind of Glial cells which are star shaped brain cells in cerebrum called Astrocytes. Like other primary brain tumors, Astrocytoma does not usually expand outside the brain and spinal cord. With this virtue, it does not have a tendency to affect other parts of the body. Young adults and children are common targets for Low-Grade Astrocytoma while

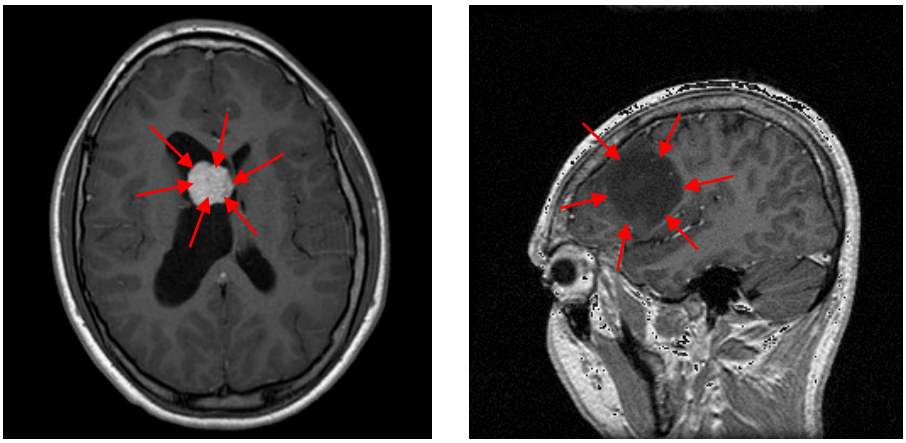

Fig. 1.5 Astrocytoma brain tumors

High-Grade Astrocytoma is more predominant among adults.

1.1.1.3 NORMAL BRAIN REGION (NORM)

The Normal regions (NORM-Class 3) are marked from these 105 images to have variant data of white matter and gray matter. T1 images are especially used to distinguish gray and white matter where gray matter is dark gray (iso to hypo), white matter is light gray (hyper). The normal region gets disarticulated due to spreading of the tumor and leakage of

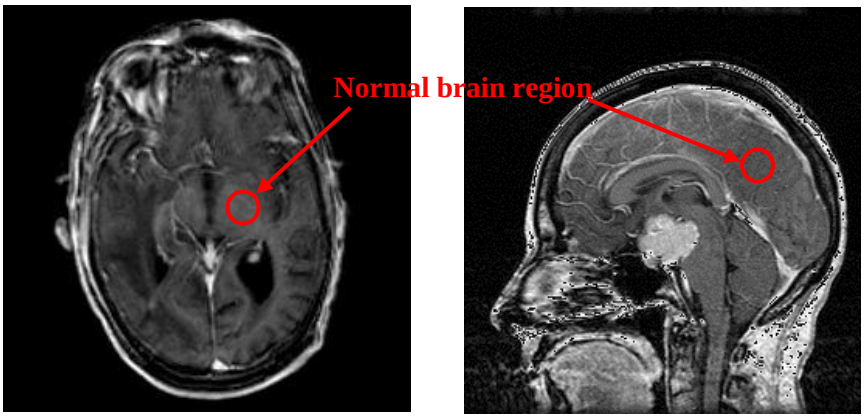

Fig. 1.6 Normal brain regions

cerebrospinal fluid (CSF). The regions near to tumor are marked specifically as the ad-joint normal area shows a bit similar properties to that of tumor. Therefore, radiologists and neurosurgeons find it difficult to locate the exact boundary of tumor.

1.1.2 SECONDARY BRAIN TUMORS

The secondary brain tumors are also called Metastatic (METS) whichspreads from other cancerous locations in the body (metastasizing) through the bloodstream or lymphatic system to another body part as the brain. Secondary brain tumors are more common than primary brain tumours.

The spreading from an annoying location to the brain is called unknown primary (CUP) origin. In growing stage, secondary brain tumours puts pressure on adjacent cells of the brain. The primary cancer site for secondary brain tumor is not in brain. These tumors grow in another part of the body then metastasized to the brain through bloodstream. The metastasizing occurs whenever cancerous cell splits from primary tumor. After breaking away from primary tumor, these cancerous cells commonly target cerebral hemispheres or cerebellum. The central spine can also be infected from secondary tumors (metastatic spine tumors). Approximately 10-20% of metastatic brain tumors are single. It is not necessary that only one Metastatic tumor can exist, there can be multiple Metastatic tumors in a patient in several different areas of the brain.

Fig. 1.7 Metastatic brain tumor

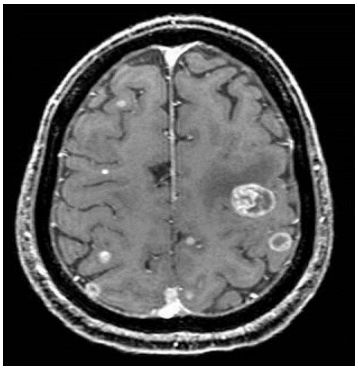

Various noninvasive imaging techniques are being utilized for visualizing soft tissue structure of brain and other parts of the body. With the help of these techniques doctor, radiologists and researchers are capable to analyze brain functionality. One of the prominent cause of death in humans is the brain tumor. The person affected from brain tumor may be relieved from mental pressure and pain by timely and proper diagnosis. The brain tumor classification is always a confrontation task for radiologists. A wrong diagnosis can lead to awful results such as paralysis, motor organ problems like problems during movement of motor organ, hearing problems etc. The large variance in tumor tissues and adjacent healthy tissues makes diagnosis a very difficult task. Its diagnosis is also a hideous task due to large variance in tumor cells and its infiltration in adjacent cells. The diagnosis of brain tumor is complex also because of complexity of tumor classification by radiologists due to its similarity in size, shape, location, intensity and texture of tumorous tissues with the adjacent healthy tissues. Though many alternatives such as meditation and surgery in the field of medical science has already been developed. However, brain tumor surgery is a crucial task because of sophisticated interconnected configuration. In spite of having these alternatives, further assistance is always a requirement for easing up the radiologists in the diagnosis process. A similar initiative is being presented in this study by developing a CAD system to classify brain tumors on post-contrast T1 MR-images. These images are obtained by introducing gadolinium material which enhances contrast. Typically, 0.15-0.20 mMol/kg gadolinium is

introduced in patients for contrast enhancement. This results a considerable contrast difference between fluid and solid anatomical structures within the body. Post-contrast T1-weighted MR images are taken as a database for better and large feature bank extraction based on intensity and texture discrimination. There are many techniques used for visual analysis of brain and other body parts also. Among those techniques, few techniques are mentioned as following:

a. Positron Emission Tomography (PET)
b. Computer Tomography (CT-scan)
c. Magnetic Emission Tomography (MRI)

1.2 MAGNETIC RESONANCE IMAGING (MRI)

Magnetic Resonance Imaging (MRI) is one of the medical imaging technique used for analysis of soft tissue anatomy of any part of body. It is also known as Nuclear Magnetic

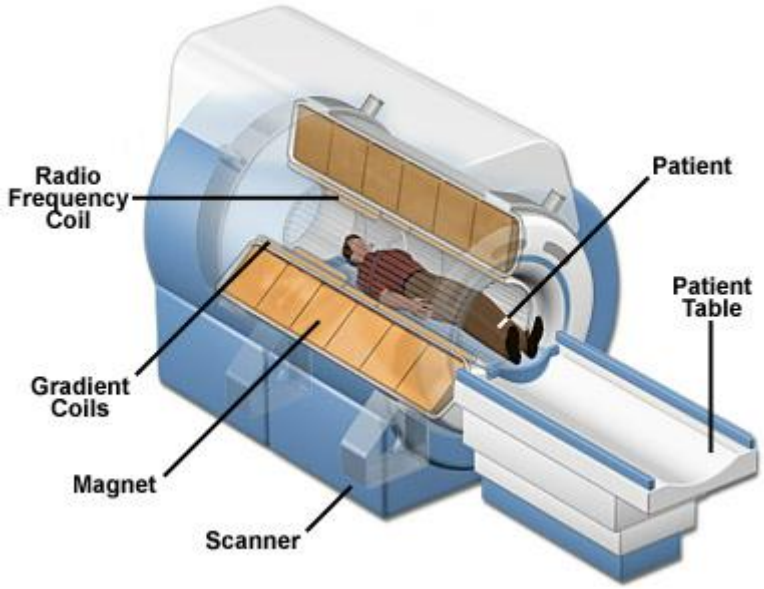

Fig. 1.8 Cutaway of MRI scanner

Resonance (NMR). The radiologists has been benefited from MRI as it is used to study and analysis of the behaviour of internal structure. MRI provides a better information about soft tissue structure of the body. Magnetic field, radio frequency and computer are used in MRI to visualize soft tissue structure of the human body. MRI is one of the extremely sensitive and complex technique test. Powerful magnetic field of 1.5 tesla (T) changes the alignment of hydrogen atoms or photons in water present in the body. Then radio frequency (RF) electromagnetic fields are used, hydrogen nuclei generates a rotating magnetic field which can be detectable by the scanner. Protons have a tendency to absorb energyat a particular frequency and after absorbing these can re-emit that absorbed energy. A surrounding coil is placed around the head to measure the net magnetization. There are two coils in it which is built in one coil itself to receive and transmit. First is transmitter coil which produces electromagnetic waves, these wave travels through the body and second is receiver coil to receive the emitted absorbed electromagnetic waves. At last computer is used to reconstruct this received signal into an image. These images has extremely good resolution which depends on relative strength, frequency, and phase of the signal produced by different type of tissues.

MRI working is a four step process and they are as:

(i) Polarization

(ii) Excitation

(iii) Precession

(iv) Relaxation.

Polarization illustrates the equilibrium tendency of nuclear magnetic moments to align parallel with an external magnetic field; *excitation* explains how an aggregate net magnetization of a collection of nuclear spins can be tipped out of equilibrium by the application of a radiofrequency (RF) electromagnetic wave pulse; *precession* depicts how non-equilibrium magnetization resonates with the magnetic field and *relaxation* describes how the magnetization returns to equilibrium. [3]

1.2.1 POLARIZATION

We know that the origin of magnetism lies in the movement of the electrically charged particles. In addition to the motion of the electrons around the nucleus, the nucleus itself rotates around its axis giving rise to a small magnetic fields as shown in Fig 1.9. It is magnetic moment that is used for acquiring magnetic resonance (MR) images. Interestingly,

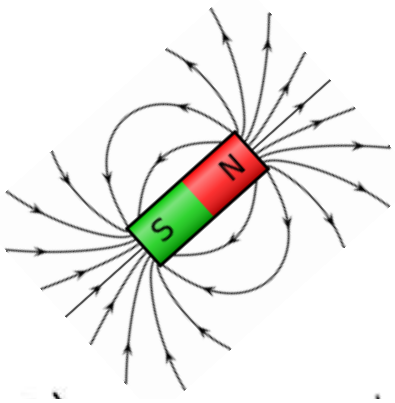

Fig 1.9 Nuclear magnetism

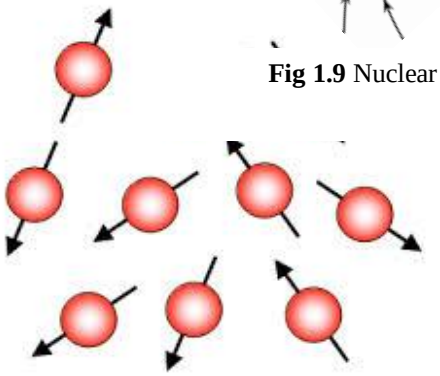

Fig 1.10 Randomly aligned nuclear spins without external field

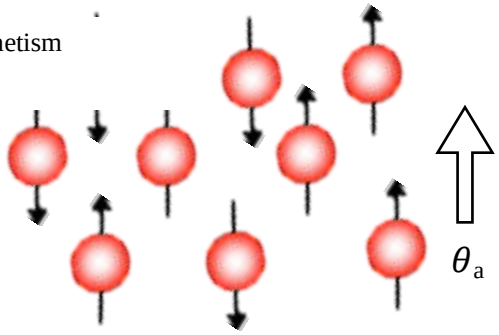

Fig 1.11 Nuclear momentalignment under
Magnetic field

net nuclear magnetism is present only when the number of protons is odd and the number of neutrons is even, such as H^{1}, N^{15}, F^{19}, Na^{23}, P^{31} or in case the number of protons is even but the number of neutrons is odd, as in case of C^{13}. Of all these elements, protons or

nucleus of H^1 is considered to be an ideal candidate of MR imaging. It is abundantly available in all living matter and its nuclear magnetism is stronger than that of any other element and hence it is easily detectable.Most commonly used protons for MR imaging are to be found in water or lipid molecules. These Lipids are a wide group of naturally-occurring molecules which includes waxes, fat, fat-soluble vitamins etc. It may be mentioned here that the magnetic moment from an individual nucleus is not detectable. Under normal circumstances, the nuclear spins in any biological matter are randomly aligned and hence the net magnetization is zero. However, when the biological matter is put under a magnetic field of strength typically denoted by B_0, the spin of all H_1 nuclei align either along or against magnetic field. Typically a B_0 of 21.5 tesla is used for clinical imaging techniques. Earth's magnetic field is of order of 0.0001 T.

1.2.2 EXCITATION

In the presence of static magnetic field, the nuclei of hydrogen i.e. protons, get divided into two groups, each having a distinct energy level, say E_1 and E_2 as shown in Fig 1.12. A

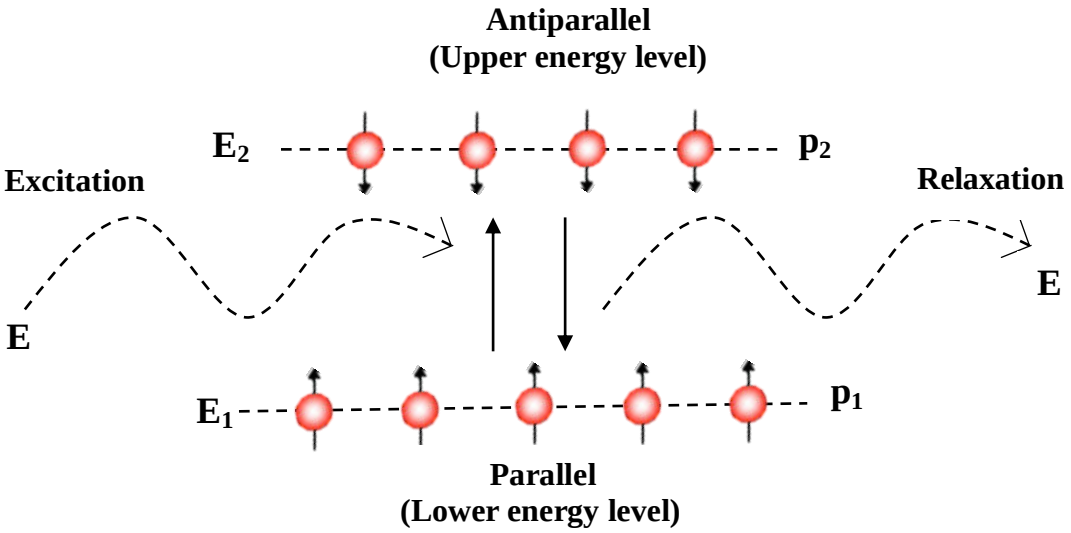

Fig 1.12 Two distinct energy levels of hydrogen nuclei

larger population of hydrogen nuclei get aligned along with the magnetic field and thus acquires lower energy level E_1, while a relatively smaller number of hydrogen nuclei align against the magnetic field and acquire higher energy level E_2. The number of protons, i.e. hydrogen nuclei in energy states E_1 and E_2 are p_1 and p_2, respectively. It may be noted that while E_1 is lower than E_2, p_1 is larger than p_2. As the magnetic strength B_0 increases, it results in a linear increase in the energy difference between E_2 and E_1. This energy difference is denoted by ΔE. Thus $\Delta E=E_2-E_1$.The proton can jump if from energy level E_1 to E_2 if the

receive an external energy greater than equal to ΔE. This is done by making RF signals incident to these polarized protons. The jump in energy level to higher one is called *excitation.*

1.2.3 PRECESSION

So far it is understood that in the absence of an external magnetic field, the spins of hydrogen nuclei are randomly oriented, but when they are placed in a strong magnetic field, say, the z-axis, a small fraction of the spin align with the axis of the applied field and a smaller fraction opposite to it, resulting in a net magnetization, M_z in the longitudinal direction (z-axis). The proton with spin parallel to the magnetic field are in lower energy state E_1 and this state called the *equilibrium state,* while the protons with spin anti-parallel to magnetic field are inhigher energy state E_2; also called *excited state*.In excited state, along with a component of the magnetic movement is in the direction of z-axis, the total magnetic movement M has a component M_{xy} too, that is the transverse component of magnetic movement in x-y plane. On account of this, the total magnetic moment precesses around z-axis with a frequency which is directly proportional to the applied magnetic field B_0. This is shown in Fig 1.13.

This behaviour is termed as Larmor frequency. It is on account of this precession that the energy is more in this state. The frequency of Larmor precession is proportional to the applied magnetic field strength as defined by the Larmor frequency (ω_0). Further $\omega_0 = \gamma B_0$, where $\gamma$is the gyromagnetic ratio.The gyromagnetic ratio is a nuclei-specific constant. For hydrogen, $\gamma = 42.6\ Mhz/T$. It may be recalled that the applied magnetics for the most of the clinical applications is 1.5 T. For this magnetic field, the Larmor precession frequency comes out to be $42.6 \times 1.5 = 63.9\ Mhz$. This is in the ratio frequency range. The energy of the photon of this ratio frequency is $h\omega_0$, where h is Plank's constant and is equal to ΔE

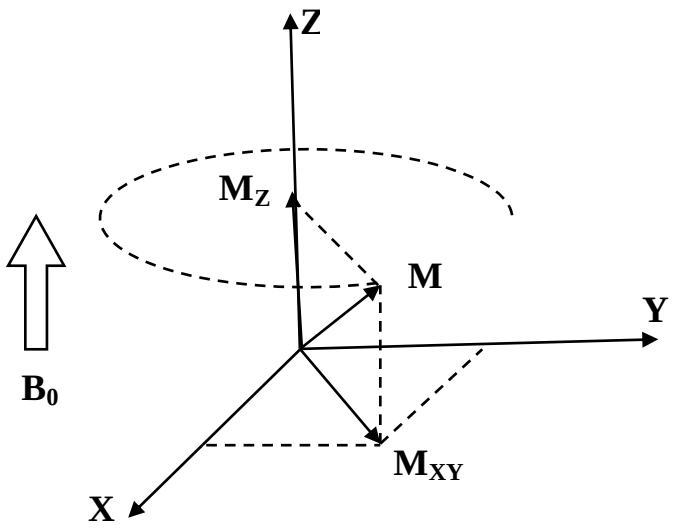

Fig 1.13 Precession of magnetic vector about the appliedmagnetic field

described earlier. Since the Larmor frequency matches with the frequency of the photon of energy difference (ΔE), the process of excitation is called resonance and the whole imaging is called magnetic resonance imaging.

1.2.4 RELAXATION

The hydrogen nuclei are normally having problem spin orientation, but on application of external magnetic field, a smaller portion gets align to the field. This alignment is mostly parallel, with lesser energy state E_1, with a few portion in anti-parallel state having higher energy state E_2. On exciting these aligned protons with suitable RF signal, some of the protons

jump from energy state E_1 to energy state E_2. The Energy in higher state is on account of precession of the proton's magnetic spin around the z-axis. Once the RF pulse is removed, the nuclei realign themselves such that their net magnetic moment is again aligned parallel with B_0 and they come back from excited state E_2 to lower energy level equilibrium state E_1. This return to equilibrium state is referred to as relaxation. During relaxation, the nuclei lose energy by emitting their own radio-frequency signal. This signal is referred to as the free-induction decay (FID) response signal. The FID response signal is measured by a conductive field coil placed around the object being imaged. The FID response signal is measured by a conductive field coil placed around the object being imaged. This measurement is processed or reconstructed to obtain 3D grey-scale MR imaged. The clarity and the improved contrast will be obtained by using MRI scanner.

The pixel density in a scan of a given tissue type, e.g., white matte verses grey matter in the brain, depends on the proton density of the tissue; the higher the proton density, the

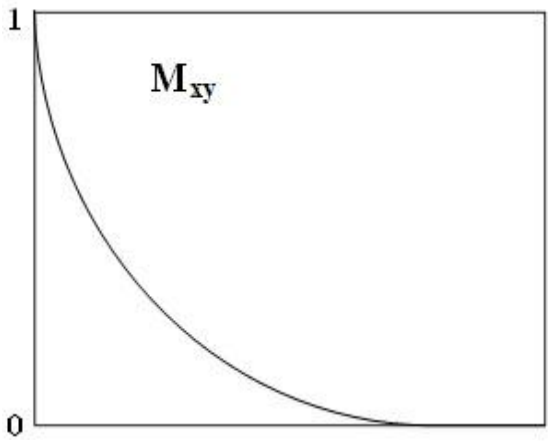

Fig 1.14 Decay M_{xy} of withtime

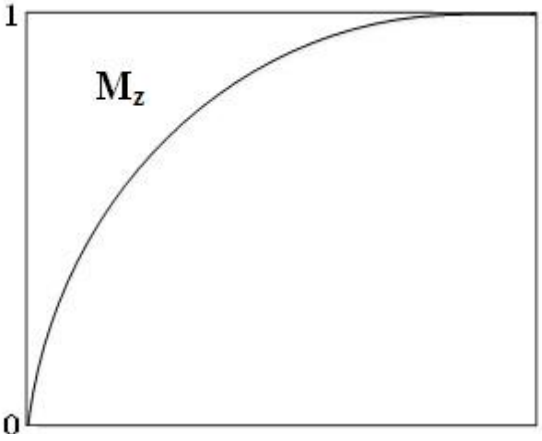

Fig 1.15 Growth of M_z with time

stronger the FID response signal. Very strictly speaking, it is the voxel density, and not the

pixel intensity, which is dependent of pixel density of the tissue. A voxel or volumetric pixel is a volume represents 2-D image data in a bitmap. This is analogous to a pixel or picture element, which depends on two other tissue-specific parameters; the longitudinal relaxation time, T_1, and the transverse relaxation time, T_2.

To understand these two times T_1 and T_2, let us revisit the concept of precession again. When the polarised protons are subjected to radio-frequency pulse, the protons acquire precession and on that account, they possess a transverse moment M_x. The longitudinal moment M_z reduces. The transverse component makes the proton spin with precession in phase with other photons. During relaxation two events occur simultaneously. One is recovery of longitudinal movement M_z, and second is the loss of coherence (getting out of phase with each other) in transverse moment M_{xy}. The exponential growth of M_z with time constant T1 is shown in Fig 1.14, while the exponentially decay of M_{xy} with time constant T_2 is shown in Fig 1.15.

MRI provides cross-sectional images of various parts of body. There are following three cross sectional planes:

a) Sagittal Plane:Sagittal plane is a vertical plane which passes from ventral (front) to dorsal (rear) dividing the body into right and left halves.

b) Coronal Plane: Coronal plane (also known as the frontal plane) is any vertical plane that divides the body into ventral and dorsal (Belly and back) sections.

c) Transverse Plane: Transverse plane (also called the horizontal plane, axial plane, or trans-axial plane) is an imaginary plane that divides the body into superior and inferior parts. It is perpendicular to the coronal and sagittal planes.

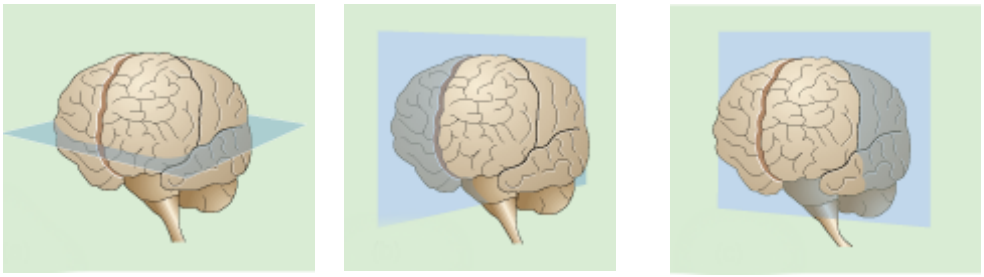

(A) Transverse plane **(B)**Sagittal plane **(C)** Coronal plane

Fig 1.16 Three cross-sectional planes of MRI

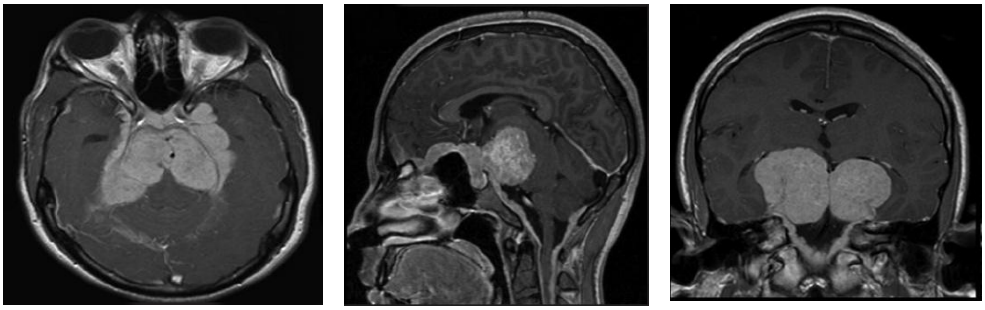

(A) Transverse plane **(B)** Sagittal plane **(C)** Coronal plane

Fig 1.17 Brain MRI images of three planes

CHAPTER 2

LITERATURE REVIEW

Many authors have proposed various algorithms for classification of brain tumors by developing various CAD systems based on different features and classification algorithm [4-7]. Generally, these systems use image processing techniques such as feature extraction, selection, and classification. The primary motive behind all these developed CAD systems is to achieve maximum accuracy. These systems used different types of brain tumor database such as MR spectroscopy, and echo planar maps related to cerebral blood volume (rCBV) along with MR imaging. The echo planar maps, MR images and MR spectroscopy are used for low grade and high grade brain tumor classification [8]. Along with these techniques, many a times MR image and perfusion data was also used for the same purpose [9] [10]. In order to classify brain tumors, researchers [11] [12] used MR spectroscopy data and got sustained results. A few conventional spectroscopic MR imaging data was exploited by Wang *et al.* to classify benign and malignant brain tumors with the help of a tree algorithm [13]. However, these signals require high-tech machines and deep knowledge of signal processing. Moreover, internet repositories do not provide such convention of signal database.

As discussed above, MRI images are of different types depending on different excitation. These excitations are T1, T2, FLAIR, and post-contrast T1. These MRI images provide different textures and intensity knowledge of brain tumor. These detailed images

differ from tumor to tumor, and relaxation time of the excited atoms. These MR images have different texture and intensity patterns for different brain tumors. The texture and intensity of these brain tumors is categorized as iso-intense, hypo intense or hyper intense. The normal brain cells and tumorous brain cells having similar signal intensity is called iso-intense while tumorous brain cells having darker signal intensity than normal brain cells, is called hypo-intense. If tumorous brain cells have brighter intensity than normal brain cells then it is called hyper-intense. Among all of these different type of MRI images, post-contrast T1 images gives better visual. The Post-contrast T1-weighted MR images are taken as a database for better and large feature bank extraction based on intensity and texture discrimination. In conventional echo repetition time (TR) (<750ms) and echo time (TE) (<40ms) and in gradient echo sequences it can be achieved by flipping angles more than 50° with TE value (<15ms). The reason for attaining these images is conventional spin echo and gradient spin echo sequences which enhances both visual interpretation as well as feature discrimination capability between different classes. Another reason for the better visual interpretation of post-contrast T1 MR-images is the injection of 0.15-0.20 ml/kg of contrast material Gadolinium into the patients. The enhancement of tumor is different for different patients in spite of the same quantity of contrast material.

These are some of previous studies which determines the clinical importance of each MR sequence. A few tumorous regions of interest (ROI(s)) are marked and segregated by radiologists and segregated through a GUI developed by the authors. Generally, there are two different ways to mark a ROI in an image. These two ways are (i) manually marking of the ROI and (ii) Through computer aided techniques. There are some researchers who have done manually marking of the ROI [14] [15]. The second method computer aided techniques can be of two types- semi-automatic marking and automatic marking. These can be also used for segregating brain tumors. The selection of a ROI segregation techniques is very hideous task as the selection of these techniques is different for different tumors. The main drawback of the automatic selection of brain tumor is its very high computational time. Hence, manually selection of ROIs is best for selecting tumorous region. Many researchers used different sizes of ROI(s) which has a considerable effect on the analysis [16, 17]. However, the final application and the feature extraction are the two factors according to which the optimal ROI size. Therefore, the examination of the influence of ROI size on texture analysis for brain tumor classification is essential. The segregated ROI should have sufficient number of pixels which gives better information. The textural feature information is highly sensitive according

to the number of pixels i.e. size of ROI. At least 800 pixels are necessary in a selected ROI to obtain the reliable result of texture analysis [18].

These are some feature which depends on the neighbor pixels as Gray Level Run-Length Matrix (GLRLM), Gray Level Co-Occurrence Matrix (GLCM). Haralick, Shanmugum, R M K, and Dinstein I [19] introduced GLCM approach in 1973. The GLCM feature matrix is most commonly used in feature extraction by many researchers. Five different features are extracted from GLCM matrix with various offsets and two different statistical features were extracted by Selveraj *et al.* [20] to differentiate abnormal and normal brain tumors. Kharrat *et al.* [21] extracted 44 features from GLCM matrix and separated tumorous regions and non-tumorous regions. 100 Features are also extracted by Zarchari *et al.* [22] where in these features are extracted from GLCM, intensity, Gabor, statistical, and shape based techniques. Like these researches, 22 features from GLCM matrix, 4 different features from the histograms, and 10 features from run-length matrix were extracted by Georgiadis *et al.* [23, 24].

After feature extraction, classification of ROIs has to be done in which certain researchers differentiate between normal or non-tumorous class and abnormal or cancerous class. Selvaraj *et al.* [20] used Least Square Support Vector machine (SVM) for the classification of 1100 cancerous and non-cancerous ROI(s) with an accuracy of 96% and 98% respectively. Another multiclass brain tumor classification has been done in two studies by Georgiadis *et al*. [23, 24] with the help of Least Square Feature Transformed-Probabilistic Neural Network (LSFT-PNN). PNN has fast training speed with less computational load as compared to other classifiers. These studies have been performed on Gliomas, Metastatic and Meningioma brain tumors. Initially first study has been done on a 75 image database of these brain tumors with a 96.67% accuracy for Glioma, 95.24% accuracy for Meningioma, and 87.50% accuracy for Metastatic brain tumors. The second study has been done on a 67 image database. This study has two stages. In the first stage primary brain tumors and secondary brain tumors are classified with an accuracy of 95.24% and 93.48% respectively while in the second study only primary brain tumors (Glioma and Meningioma) are considered which delivers 88.89% accuracy for Gliomas and 100% accuracy for Meningiomas.

Similar study has been performed by Zacharaki *et al.* [22] with 98 images of Glioblastoma Multiforme, Low Grade Glioma, and Metastatic brain tumors. The main objective of this study is the brain tumor grade and type classification with the help of MRI texture. In this study an automated modality has been developed to help in the visual analysis of the neoplasms in the brain. This visual analysis is based on defining the grade and type of

the brain tumors. An investigation has also been done on the uses of the pattern classification method to classify different brain tumor type. An accuracy of 90.9% for Low-Grade Glioma, 91.7% for Metastases and 41.2% for Glioblastoma Multiforme has been achieved.

Kumar *et al*. [25] studied 428 post contrast T1-images of different types of primary brain tumors and secondary brain tumors. This study had been done to aid radiologist(s) in evolution of brain tumors and in detecting tumor boundaries of various tumors. The Gradient Vector Flow (GVF) which is an edge based technique was used to segregate primary and secondary brain tumor from normal tissues. GVF has a user friendly model for segregation of ROI(s). A total of 856 ROI(s) have been segregated from the dataset. A total of 218 features have been extracted from each ROI. A Principle Component Analysis (PCA) has been used to reduce the feature vector dimensionality. After reduction of the feature vector, it is given as an input to the Artificial Neural Network (ANN) for the classification of brain tumor. Astrocytoma (AS), child tumor-Medulloblastoma, Meningioma (MEN), Glioblastoma Multiforme (GBM), (MED), and secondary tumor- Metastatic (MET) with normal region (NR) were discriminated using Artificial Neural Network (ANN). This study has 90.74% accuracy for Astrocytoma, 88.46% accuracy for Glioblastoma Multiforme, 90.70% accuracy for Meningioma, 85.00% accuracy for Medulloblastoma, 96.67% accuracy for Metastatic and 93.78% for Normal Region. This approach has an overall accuracy of 72.97% - 95.37%.

Sachdeva *et al.* [26] had also developed a Computer Aided Technique (CAD) system in order to aid radiologist(s) for multiclass brain tumor classification. In this study, 428 post contrast T1- weighted MR images of 55 patients had been taken as a database. This database has MR-images of the child tumor named Medulloblastoma (MED), Meningioma (MEN), Glioblastoma Multiforme (GBM), Astrocytoma (AS), and secondary tumor- Metastatic (MET) with normal region (NR). The Content Based Active Contour (CBAC) has been used for the segregation of ROI(s). A total of 218 texture and intensity features were extracted from the ROI(s). Genetic algorithm was used to select optimal features. This optimal set of features are then given to the Support Vector Machine (SVM) classifier. An overall accuracy of 91.7% was achieved using SVM technique. An individual class accuracy of 97.1% for Medulloblastoma, 96% for Meningioma, 83.3% for Glioblastoma Multiforme, 89.8% for Astrocytoma, and 91.8% for Metastatic brain tumors was achieved.

Al-Shaikhli *et al.* [27] performed a different study on a database which has 50 normal brain images, 50 Glioma brain tumor images, 50 Glioblastoma brain tumor images, and 50 images of Metastatic brain tumor. This database was experimented with dictionary learning

and sparse coding classifier which has K-SVD algorithm. An overall accuracy of 93.75% was achieved with this method.

It is being observed that there are only few researchers who have done the classification of Meningioma and Astrocytoma together with Normal brain MR-images. Mostly researchers classified Glioma, Meningioma, and Metastatic brain tumors. These brain tumors are easily classified as they have distinctive features. Besides this, a very few features were extracted and as a result low accuracy were obtained. No attempts have been made to include LAW's textural energy measures (LTEM) in feature bank to classify brain tumors. A very few studies have been done on classification of Meningioma and Astrocytoma brain tumors with lower classification accuracy due to their similar textural and intensity patterns.

In this research, these above limitations are surmounted with the help of GUI developed for ROI segregation. 371 texture and intensity features are obtained from the ROI(s) segregated from the post-contrast T1 weighted MR-images from 10 patients. Initially, ANN classifier is used to test these ROI(s) with limited number of features excluding LTEM features. LTEM features are then added to obtain more accuracy with ANN classifier. Different experiments have been performed on these two experimental setup for three classes: Meningioma (MENI- Class 1), Astrocytoma (AST- Class 2) and Normal brain region (NORM class-3). The CAD system can be applied further to (i) deliver extra reliable differentiation, especially with similar tumors (ii) expedite the diagnosis.

Table 2.1 Overview of the previous brain tumor classification methods

The CAD system consists of three major parts: ROI(s) selection, intensity and texture feature extraction, and classification of brain tumors based on ANN. The feature extraction includes First Order Statistics (FOS), Gray Level Co-occurrence Matrix (GLCM), Gray Level Run Length Matrix (GLRLM), LAW's Texture Energy Measure (LTEM), and Gabor Filters (GWT). These intensity and texture features plays a crucial role in discriminating different brain tumor classes.

S. NO.	AUTHOR	BRAIN TUMOR	NUMBER OF	INDIVIDUAL CLASS ACCURACY	OVERALL

	(YEAR)	CLASSES	FEATURES	BRAIN TUMOR	ACCURACY	CLASSIFICATION ACCURACY
1.	**Selveraj (2007)**	Normal and abnormal slices of brain MR-images	5 GLCM features from different offsets and 2 statistical features	Normal Abnormal	96% 98%	97%
2.	**EI Dashan (2010)**	Normal and abnormal slices	Discrete Wavelet Transform features	Normal Abnormal	97% 98%	97.5%
3.	**Kharrat (2010)**	normal regions, benign and a malignant tumors	44 GLCM features	Normal Benign Malignant		94.44%
4.	**Zarchari (2010)**	Low Grade Gliomas, Glioblastoma Multiforme, Metastatic	100 features from GLCM, Gabor, shape and statistical feature extraction techniques	Low-grade Gliomas Glioblastoma Multiforme Metastatic	90.9% 33.4% 91.7%	72%
5.	**Georgiadis (2008)**	Metastases, Meningiomas Gliomas	4 features from histograms, 22 features were extracted from the GLCM and 10 features were extracted from the run-length matrices	Metastases, Meningiomas Gliomas	87.50% 95.24% 96.67%	93.14%
6.	**Sachdeva (2011)**	Astrocytoma Glioblastoma Multiforme Medulloblastoma Meningioma Metastatic Normal regions	218 intensity and texture features	Astrocytoma Glioblastoma Multiforme Medulloblastoma Meningioma Metastatic Normal regions	90.74% 88.46% 85% 90.70% 96.67% 93.78%	85.23%
7.	**Present study (2015)**	Meningioma Astrocytoma Normal Brain	371 intensity and texture features Using GLCM, GLRLM, GABOR, LTEM, FOS Techniques	Meningioma Astrocytoma Normal Brain	91.40% 91.43% 94.29%	92.43%

CHAPTER 3

METHEDOLOGY

3.1 OBJECTIVES

The objectives which will be followed are:

a) Data collection of primary tumors that originate in the brain itself like
   i. Astrocytoma (AST)
   ii. Meningioma (MENI)
   iii. Normal brain (NORM)
b) Segregating tumor boundaries regions of interest (ROIs) from the MR-images which will constitute:
   i. Extraction of intensity and texture based features from ROI(s)
   ii. To remove redundant features by applying feature selection technique where only those features are left with discriminatory information
   iii. Classification by Artificial Neural Network (ANN)

3.2 PROPOSED METHODOLOGY

In this methodology, a Computer Aided Diagnostic (CAD) system will be developed (shown in Fig 3.1) to differentiate three types of brain tumors with higher classification accuracy. The CAD system developed by authors overcomes earlier limitations in multi-class classification of brain tumor. It dwells three main parts which are as following:

a) Segregating ROI (s) from database
b) Intensity and texture feature description
c) ANN classifier with features as input

3.3 SELECTION OF REGION OF INTEREST (ROI)

A secondary database of ROI(s) is obtained by developing a GUI using MATLAB 2015a which guides the user to mark as well as segregate the region of interest from the main image. These ROI(s) are a sub part of main image in medical imaging. A ROI has the fundamental diagnosis information which can be used for computations and diagnosis process. Depending on the methodology used, optimal size of the ROI varies. The ROI size also depends on the application for which it will be used. Either too large ROI like 40×40 or too small ROI like 10×10 does contain too much or too less information for computation respectively[28].

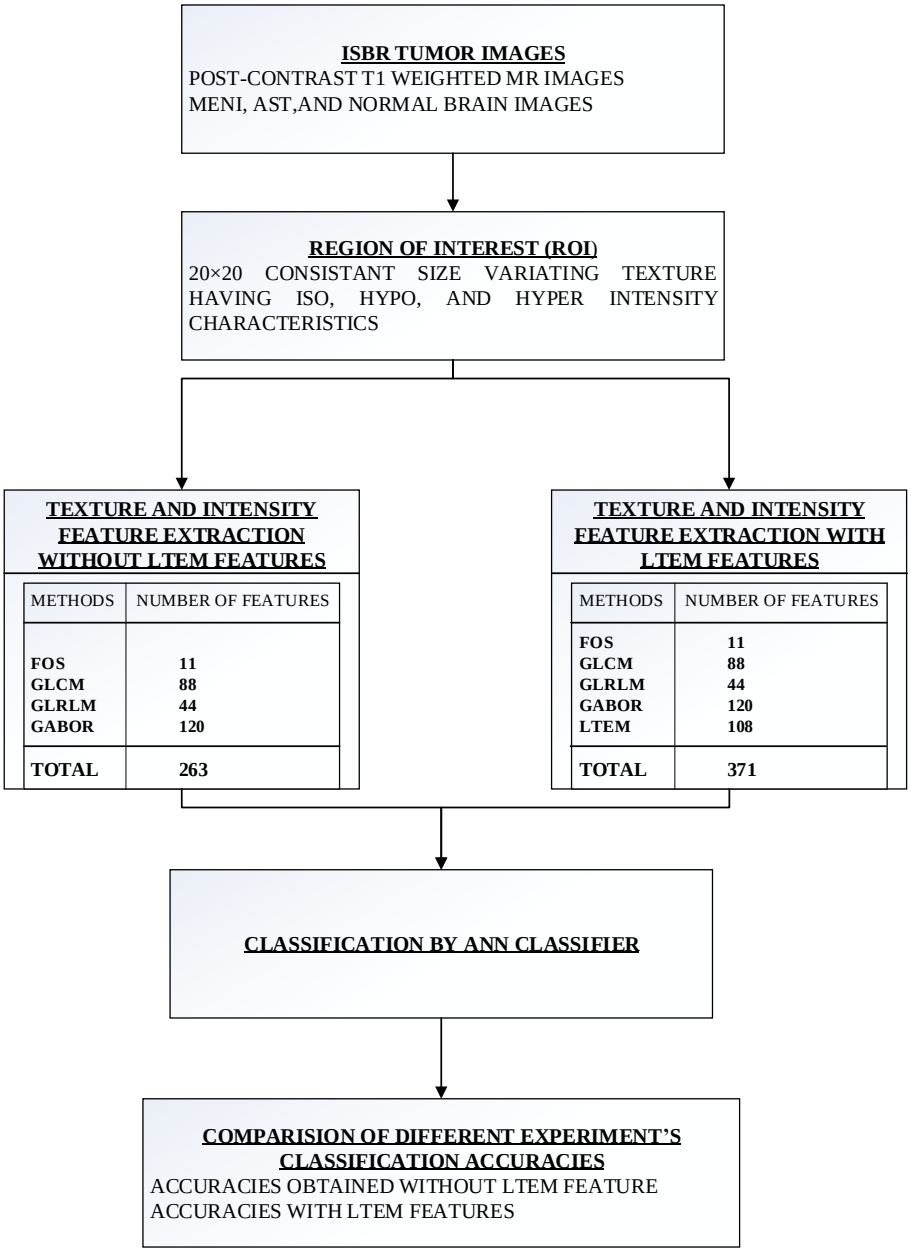
ISBR TUMOR IMAGES
POST-CONTRAST T1 WEIGHTED MR IMAGES
MENI, AST,AND NORMAL BRAIN IMAGES
REGION OF INTEREST (ROI)
20×20 CONSISTANT SIZE VARIATING TEXTURE HAVING ISO, HYPO, AND HYPER INTENSITY CHARACTERISTICS
TEXTURE AND INTENSITY FEATURE EXTRACTION WITHOUT LTEM FEATURES
METHODS
NUMBER OF FEATURES
FOS 11
GLCM 88
GLRLM 44
GABOR 120
TOTAL 263
TEXTURE AND INTENSITY FEATURE EXTRACTION WITH LTEM FEATURES
METHODS
NUMBER OF FEATURES
FOS 11
GLCM 88
GLRLM 44
GABOR 120
LTEM 108
TOTAL 371
CLASSIFICATION BY ANN CLASSIFIER
COMPARISION OF DIFFERENT EXPERIMENT'S CLASSIFICATION ACCURACIES
ACCURACIES OBTAINED WITHOUT LTEM FEATURE
ACCURACIES WITH LTEM FEATURES

Fig. 3.1 Block diagram of the CAD system for brain tumor classification

A comparative analysis has been performed on various sizes 40×40, 30×30, 20×20 of ROI(s) segregated from a particular image from database as shown in Fig. 3.2. This comparative analysis has been done on these ROI(s) which is based on plotting box plots in Matlab2015a. These box-plots are based on two different features which are contrast and difference entropy. MENI (class-1) and AST (class-2) have been selected for comparison with two different ROI sizes. MENI-20 signifies Meningioma with ROI size 20×20 and AST-20 means Astrocytoma with ROI size 20×20.

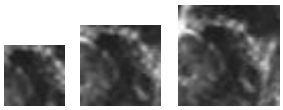

(a) **(b)** **(c)**

Fig. 3.2 Various sizes of ROIs **(a)** 20x20 **(b)** 30x30 **(c)** 40x40

It has been analysed from this comparison that the differentiation capability of ROI size 20×20 and 40×40 is almost similar. Along with differentiating two classes, ROI size of 20×20 and 40×40 contains approximately similar information within itself. It is being analysed from the Fig. 3.3 and Fig. 3.4 that MENI-20 and MENI-40 have a dominancy in lower range and AST-20 and AST-40 have dominancy in upper part. The same type of tumors show similar information except for some typical cases as stated below. The major reasons for segregating 20x 20 size ROI(s) are:

a) ROIs are marked in such a way that they cover both necrotic and cystic (heterogeneous) part of the tumor.
b) Few of the tumors show peripheral enhancement such as AST and thus cause change in the texture property of the periphery and in the region near to the periphery. ROI of 20x20 thus cover both the hypo as well as hyper region.
c) It provides less computational time and high differentiation capability.
d) Therefore, this size is found out to be appropriate for segregating ROI in this methodology.

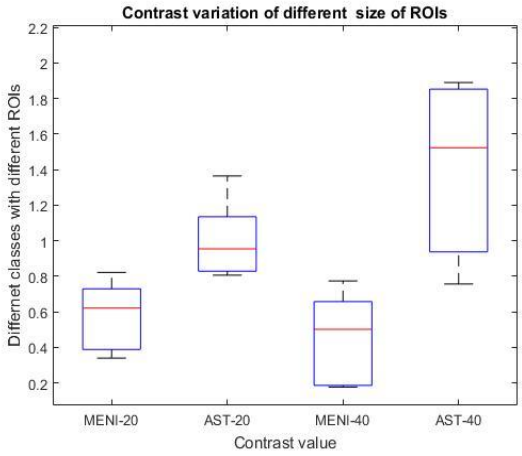

(a) **(b)**

Fig. 3.3 Box plot analysis of different parameters with dissimilar ROI sizes **(a)** Contrast value of different classes with different ROI sizes **(b)** Difference entropy values of different classes with different ROI sizes

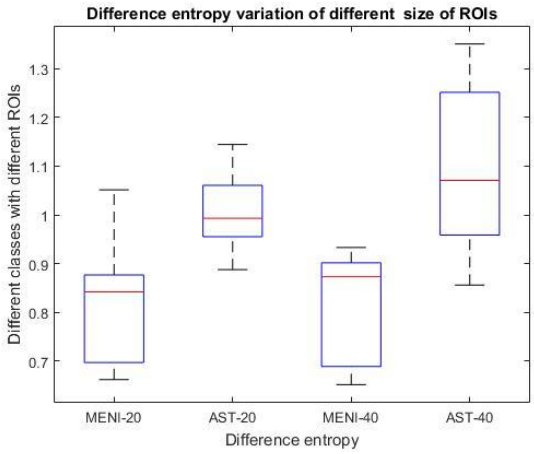

3.4 INTENSITY AND TEXTURE FEATURE EXTRACTION

The combination of intensities at a specific positions relative to each point in the image are named as features. The categorization of the features depends on the number of feature defining points of an image. These features are categorised into higher order, second order, and first order features, where higher number of feature defining points means higher order.

In the present method, ROI(s) are taken as input to feature extraction unit. initially, five different intensity and texture features of higher, second and first order statistics, spatial-filtering with law's texture energy mask, and multi-scaled and multi-resolution tuneable analysis with gabor wavelet are selected. These five methods are (i) First Order Statistics (FOS) (ii) Gray-Level Co-Occurrence Matrix (GLCM) (iii) Gray Level Run-Length Matrix (GLRLM) (iv) Texture Energy Measures (LTEM) and (v) Gabor Wavelet (GWT). There are various studies [29, 30] in which a combination of these features has been used. The feature

selection is based on these studies and the type of information it provides. A total of 371 visual and non-visual texture and intensity features are extracted and then applied to present classification cad system. These methods have one extracted feature set for each hence total five feature sets are obtained from five methods. These sets were concatenate into one feature set named as feature vector. Further, this feature vector is used for characterization of image. These five textural features are:

3.4.1 FIRST ORDER STATISTICS (FOS)

The First Order Statistics (FOS) computes various values at individual pixels of an image and hence FOS examines the spatial distribution of gray levels in an image. Let A(x, y) is an image with 'I' representing the gray levels then first-order histogram P (I) is defined as:

$$P(I) = \frac{\text{Number of pixels with gray level 'I'}}{\text{Total number of pixels in an image}}$$

A total 11 features has been extracted where skew-ness, variance, and kurtosis are computed most frequently. There are which are being extracted from various segregated ROI's and those features are:

a) MINIMUM GRAY LEVEL: $f_1 = \min [A(x, y)]$

b) MAXIMUM GRAY LEVEL: $f_2 = \max [A(x, y)]$

c) MEAN GRAY LEVEL:

$$f_4 = \sum_{i=0}^{N_g - 1} i.P(I)$$

d) STANDARD DEVIATION OF GRAY LEVEL:

The deviation of the gray levels from the mean value is the measure of histogram width which is also called variance. The square root of the variance is the standard deviation. It is defined as:

$$f_5 = \sqrt{\sum_{i}^{N} (g - f_4)^2 P(I)}$$

e) COEFFICIENT OF VARIATION:

$$f_6 = \frac{f_5}{f_4}$$

f) GRAY LEVEL SKEWNESS:

The symmetry of a gray level histogram around the mean value is called gray level skewness which is defined as:

$$f_7 = \frac{1}{{f_5}^3} \sum_{i} (i - f_4)^3 P(I)$$

g) GRAY LEVEL KURTOSIS:

Gray Level Kurtosis is the flatness of the histogram. It is defined as:

$$f_8 = \frac{1}{{f_5}^4} \sum_{i} (i - f_4)^4 P(I) - 3$$

h) GRAY LEVEL ENERGY:

$$f_9 = \sum_{i} P(I)^2$$

i) GRAY LEVEL ENTROPY:

$$f_{10} = -\sum_{i} P(I) \ln P(I)$$

3.4.2 GRAY LEVEL CO-OCCURRENCE MATRIX (GLCM)

The features extracted from the FOS technique provide some information which is related to the gray-level distribution of an image. However, features extracted from FOS technique do not have any kind of information about the gray level pairs and relative positions within an image. These extracted features are not able to measure the position of low value gray levels or any high value gray levels. The repetitive or occasional occurrence of some of the gray-level pair can be explained by a GLCM matrix of frequencies$P_{\theta,d}(I1, I2)$. This GLCM matrix explains the frequency of two pixels occurrence in a window with distance 'd' and in 'θ' direction with gray-levels I_1 and I_2. The second order features [19, 31] are being extracted from this co-occurrence matrix where pixels are not considered individually. These pixels are considered as a pair in order to build$P_{\theta,d}(I1, I2)$. The co-occurrence matrix mainly has two parameters:

1. Relative distance which is being measured in pixel number *'d'*
2. The relative orientation 'θ' which is being quantized in four different directions.

These four directions represents anti-diagonal, diagonal, vertical and horizontal by 135°, 45°, 90°, and 0° respectively. The non-normalized frequencies of co-occurrence matrix as functions of distance, d and angle 0°, 45°, 90° and 135° can be represented respectively as:

$$P_{0^0,d}(I_1, I_2) = \left| \begin{Bmatrix} [(k,l),(m,n)] \in D \\ k - m = 0, |l - n| = d \\ f(k,l) = I_1, f(m,n) = I_2, \end{Bmatrix} \right|$$

$$P_{45^0,d}(I_1, I_2) = \left| \begin{Bmatrix} [(k,l),(m,n)] \in D \\ (k - m = d, l - n = -d) \vee (k - m = -d, l - n = d) \\ f(k,l) = I_1, f(m,n) = I_2, \end{Bmatrix} \right|$$

$$P_{90^0,d}(I_1, I_2) = \left| \begin{Bmatrix} [(k,l),(m,n)] \in D \\ k - m = d, |l - n| = 0 \\ f(k,l) = I_1, f(m,n) = I_2, \end{Bmatrix} \right|$$

$$P_{135^0,d}(I_1, I_2) = \left| \begin{Bmatrix} [(k,l),(m,n)] \in D \\ (k - m = d, l - n = d) \vee (k - m = -d, l - n = -d) \\ f(k,l) = I_1, f(m,n) = I_2, \end{Bmatrix} \right|$$

where,these four sets refers to cardinality, $f(k, l)$ is intensity at pixel position (k, l) in the image of order $(M \times N)$and the order of matrix $D$is $(M \times N) \times (M \times N)$. Using Co-occurrence matrix, features can be defined which quantifies coarseness, smoothness and texture- related information that have high discriminatory power. Let Fig. 3.5 is a matrix of the gray levels of an image and Fig. 3.6 is a co-occurrence matrix of this segment of image.

ANGLE	OFFSET
0°	[0 D]
45°	[-D D]
90°	[-D 0]
135°	[-D -D]

1	1	5	6	8
2	3	5	7	1
4	5	7	1	2
8	5	1	2	5

Fig. 3.5 Gray scale value matrix

	1	2	3	4	5	6	7	8
1	1	2	0	0	1	0	0	0
2	0	1	1	0	1	0	0	0
3	0	0	0	0	1	0	0	0
4	0	0	0	0	1	0	0	0
5	1	0	0	0	0	1	2	0
6	0	0	0	0	0	0	0	1
7	2	0	0	0	0	0	0	0
8	0	0	0	0	1	0	0	0

Fig. 3.6 Co-occurrence matrix (GLCM)

The GLCM matrix has the number of occurrence of a particular pixel pair in an image. These pixel pairs are indicated as (i, j). The GLCM matrix indicates the horizontal repetition of a pixel with a value i adjacent to another pixel having value j. It is clear from the above figure that the occurrence of pixel pair (1, 1) is only one time and the repetition of pixel pair (1, 2) is two times. These repetitions are clearly defined by the GLCM matrix. The distance D (which is generally defined by offset) and angle θ within a given neighborhood are used for calculation of probability distribution between pixels. The various offsets and the relative angles are defined as:

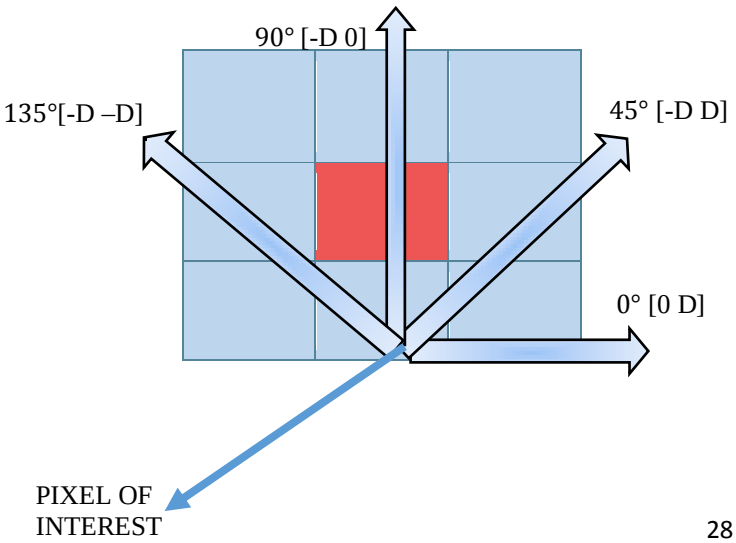

Fig. 3.7 Different orientation of the GLCM matrix

a) ANGULAR SECOND MOMENT (ASM):

Angular Second Moment (ASM) is the measure of homogeneity or smoothness of an image. The less smooth the ROI is, the more uniformly distributed$P_{\theta,d}(I1, I2)$and the lower will be the value of ASM. A homogeneous image has only few gray levels. These few gray levels gives a GLCM matrix with few but relatively very high values from $P(i,j)$. Thus, the ASM will be high. It is defined as:

$$ASM = \sum_{i=0}^{G-1}\sum_{j=0}^{G-1}\{P(i,j)\}^2$$

b) CONTRAST (CON):

The information regarding the sudden change in the intensity values of an image is the measure for contrast value of that image. The contrast value is also ameasure of local difference which gives high value for a high contrast image. The contrast is defined as:

$$CON = \sum_{n=0}^{G-1}(n)^2 \sum_{i=1}^{G}\sum_{j=1}^{G}\{P(i,j)\}, |i-j|=n$$

c) INVERSE DIFFERENCE MOMENT (IDM):

Inverse Difference Moment (IDM) is affected by the homogeneity (ASM values) of an image. The weighting factor $[1+(i-j)^2]^{-1}$ is the main reason for the influence of homogeneity on IDM values. The non-homogeneous regions $(i \neq j)$ contribute a little for the better IDM values. A high value result indicates a homogeneous region of an image where low value results indicates non-homogeneous region of an image. IDM is defined as:

$$IDM = \sum_{i=0}^{G-1}\sum_{j=0}^{G-1}\frac{1}{1+(i-j)^2}P(i,j)$$

d) ENTROPY (ENT):

Entropy (ENT) is one of the statistical measure of the randomness which is used to categorise an image texture. An image with a black sky is considered as low entropy image as it does not has randomness. A perfect flat image has zero entropy. An image which has the information of moon surface is a high value of entropy as it has a lot random values. ENT is defined as:

$$ENT = -\sum_{i=0}^{G-1}\sum_{j=0}^{G-1} P(i,j) * \log(P(i,j))$$

e) CORRELATION (COR) :

Correlation (COR) is the measure of gray levels linear dependence between the pixels at a specified positions relative to one another. COR values defines an association of different pixels in two diverse orientation. It is defined as:

$$COR = \sum_{i}\sum_{j} \frac{(i.j)\, P(i,j) - \mu_x \mu_y}{\sigma_x \sigma_y}$$

f) SUM OF SQUARES (VARIANCE) (VAR):

This feature puts relatively high weights on the elements that differ from the average value of $P(i,j)$. It is defined as:

$$VAR = \sum_{i=0}^{G-1}\sum_{j=0}^{G-1} (i - \square)^2\, P(i,j)$$

g) SUM AVERAGE (SA):

$$SA = \sum_{i=2}^{2N_g} i.\ P_{x+y}(i)$$

h) SUM VARIANCE (SV):

$$SV = \sum_{i=2}^{2N_g} (i - f_8)^2 .\ P_{x+y}(i)$$

i) SUM ENTROPY (SE):

$$SE = -\sum_{i=0}^{2N_g} P_{x+y}(i)\{logP_{x+y}(i)\}$$

j) DIFFERENCE VARIANCE (DV):

$$DV = variance\ of\ P_{x-y}$$

k) DIFFERENCE ENTROPY (DE):

$$DE = -\sum_{i=0}^{N_g-1} p_{x-y}(i) \log\{p_{x-y}(i)\}$$

l) AUTOCORRELATION (ACR):

$$ACR = \sum_{i=0}^{G-1}\sum_{j=0}^{G-1} (i,j)\, P(i,j)$$

m) DISSIMILARITY (DSS):

$$DSS = \sum_{i=0}^{G-1}\sum_{j=0}^{G-1} |i-j| . P(i,j)$$

n) CLUSTER SHADE (CHS):

$$CHS = \sum_{i=0}^{G-1}\sum_{j=0}^{G-1} (i + j - \mu_x - \mu_y)^3\, P(i,j)$$

o) CLUSTER PROMINANCE (CP):

$$CP = \sum_{i=0}^{G-1} \sum_{j=0}^{G-1} (i + j - \mu_x - \mu_y)^4 \, P(i,j)$$

p) MAXIMUM PROBABILITY (MP):

$$MP = \max_{i,j} P(i,j)$$

Together all these features provide high discriminative power to distinguish two different kind of images. All features are functions of the distance *d* and the orientation θ. Thus, if an image is rotated, the values of the features will be different. In practice, for each *d* the resulting values for the four directions are averaged out. This will generate features that will be rotations invariant.

3.4.3 GREY LEVEL RUN LENGTH MATRIX (GLRLM)

Galloway proposed the usage of the run-length matrix for textural analysis [33] with an analysis that, in the coarse texture, relatively long gray-levels run would occur more frequently and a fine texture should have primarily short runs. Grey-Level Run-Length Matrix (GLRLM) is another matrix based technique which is used to extract the textural information from an image. The pattern of a particular gray value pixel from a reference pixel in a specific direction is called as texture. GLRLM matrix is based on the run length. This is described as the total number of neighbour pixels which have the similar gray value in a specific direction. The run length matrix *RL(a, b)* has two dimensions where each element of this matrix is the total number of elements *b* with a specific intensity value *a* in specific direction [34]. A total 11 number of features can be extracted form *RL(a, b).*

$$R(\theta) = \big((RL(a,b)|\theta)\big), 0 \leq a \leq N_g \, , 0 \leq b \leq R_{max}$$

where, N_g is maximum gray level and R_{max} is the maximum length. The run-length matrix calculates the run-length of a particular pixel. If a pixel has one occurrence in a particular direction is will be calculates as one run-length. If this pixels has one or more occurrence side by side it will be incremented that many times in run-length matrix as shown in Figure 3.9.

1	**2**	**3**	**4**
1	3	4	4
3	2	2	2
4	1	4	1

Fig. 3.8 Image array

Gray level	Run Length (b)			
	1	**2**	**3**	**4**
1	4	0	0	0
2	1	0	1	0
3	3	0	0	0
4	3	1	0	0

Fig. 3.9 Run-length matrix (GLRLM)

There are the few features which are being calculated from the GLRLM matrix. These features are also calculated in four directions i.e. 0°, 45°, 90° and 135°. The calculated 11 features are:

a) SHORT RUN EMPHASIS (SRE):

$$SRE = \frac{1}{n_r}\sum_{i=1}^{M}\sum_{j=1}^{N}\frac{p(i,j)}{j^2}$$

b) LONG RUN EMPHASIS (LRE):

$$LRE = \frac{1}{n_r}\sum_{i=1}^{M}\sum_{j=1}^{N}P(i.j).j^2$$

c) GRAY-LEVEL NON-UNIFORMITY (GLN):

$$GLN = \frac{1}{n_r}\sum_{i=1}^{M}\left(\sum_{j=1}^{N}P(i.j)\right)^2$$

d) RUN LENGTH NON-UNIFORMITY (RLN):

$$RLN = \frac{1}{n_r}\sum_{j=1}^{N}\left(\sum_{i=1}^{M}P(i.j)\right)^2$$

e) RUN PERCENTAGE (RP):

$$RP = \frac{n_r}{n_p}$$

f) LOW GRAY-LEVEL RUN EMPHASIS (LGRE):

$$LGRE = \frac{1}{n_r}\sum_{i=1}^{M}\sum_{j=1}^{N}\frac{p(i,j)}{i^2}$$

g) HIGH GRAY-LEVEL RUN EMPHASIS (HGRE):

$$HGRE = \frac{1}{n_r}\sum_{i=1}^{M}\sum_{j=1}^{N}P(i.j).i^2$$

h) SHORT RUN LOW GRAY-LEVEL EMPHASIS (SRLGE):

$$SRLGE = \frac{1}{n_r}\sum_{i=1}^{M}\sum_{j=1}^{N}\frac{p(i,j)}{i^2.j^2}$$

i) SHORT RUN HIGH GRAY-LEVEL EMPHASIS (SRHGE):

$$SRHGE = \frac{1}{n_r}\sum_{i=1}^{M}\sum_{j=1}^{N}\frac{p(i,j).\ i^2}{j^2}$$

j) LONG RUN LOW GRAY-LEVEL EMPHASIS (LRLGE):

$$LRLGE = \frac{1}{n_r}\sum_{i=1}^{M}\sum_{j=1}^{N}\frac{p(i,j).\ j^2}{i^2}$$

k) LONG RUN HIGH GRAY-LEVEL EMPHASIS (LRHGE):

$$LRHGE = \frac{1}{n_r}\sum_{i=1}^{M}\sum_{j=1}^{N} P(i.j).j^2.i^2$$

3.4.4 GABOR WAVELET TRANSFORM (GWT)

Initially, the Gabor function was invented by Dennis Gabor a Hungarian electrical engineer in 1946 [35]. More recently, few methods which are based on multi-channel or multi- resolution analysis. The wavelet transform and Gabor Filters are based on these techniques. These techniques have attained much more attention for the texture analysis as texture segmentation, texture classification and related applications. The Pyramid Structured Wavelet Transform (PSWT) was initially used by Mallat (1989) for textual analysis. This initial application of the PSWT was followed by many researchers (e.g., Arivazhagan and Ganesan 2003; Manthalkar *et al.*, 2003b; Charalampidis and Kasparis, 2002; Pun and Lee, 2001; Wang and Liu, 1999; Van De Wouwer *et al.*, 1999) in the analysis of texture. The main limitation of these type of filters is the decomposition of an image into only three directional (vertical, diagonal and horizontal detailed bands in 135º, 45º, 0º directions respectively). This drawback limits the application of this transform for the rotation-invariant texture analysis.

Among the many approaches of segmentation and textual analysis, unsupervised and supervised techniques using GWT with various orientation and scale are main techniques (e.g., Idrissa and Acheroy, 2002; Pichler *et al.*, 1996; Dunn and Higgins, 1995; Teuner *et al.*, 1995; Haley and Manjunath, 1995; Bovik *et al.*, 1992; Jain and Farrokhnia, 1991; Du Buf, 1990; Fogel and Sagi, 1989; Tuner, 1986). Another technique with Rotation Invariant Gabor Filters (RIGF) are also used for texture classification by Manthalkar *et al.*, 2003a and Haley and Manjunath, 1995. An advanced technique which is a combination of RIGF and Circular Gabor Filter (CGF) was applied by Zhang and Tan, 2002.

A rotation invariance was achieved using feature element circular shift in order to achieve the same dominant direction. This was named as Rotation Normalization Method. The equality between the spatial domain rotation and the Gabor Filter element circular shift was proved by Zhang *et al.*, 2000.

The Gabor functions has various applications which includes textural classification, edge detection, face detection and segmentation. An image can be visualized with a magnification using the multi-scaled and multi-tuneable Gabor Filters. The feature extraction

with the help of Gabor Filters (GF) has an advantage that these filters have multi-tuneable and multi-scaled settings. These settings aids in finding minute textural changes in an image. Basically, GFs are a group of wavelets. These wavelets has individual energy capturing capacity at a particular scale and at a particular orientation. The Gabor wavelets are originated by the rotation and dilation in two-dimensional case of a particular Gabor function [36]. There are two types of Gabor functions based on the dimensionality, those are as following:

3.4.4.1 GABOR FILTER FUNCTIONS

a) ONE-DIMENSIONAL GABOR FILTER FUNCTION

A one dimensional Gabor Filter function is also named as harmonic oscillator. A harmonic oscillator is a complex sinusoidal plane wave which has some frequency and a specific orientation within a Gaussian envelope. Hence, the product of complex sinusoidal and a Gaussian function can be stated as Gabor function. The general one-dimensional Gabor filter function can be defined as:

$$G(x) = \frac{1}{\sqrt{2\pi\rho}} exp\left(\frac{-x^2}{2\sigma^2}\right) exp(j\pi W x)$$

where, W is the modulation frequency, σ is the Gaussian function scale, ρ is the standard deviation and the $G(x)$ is the one dimension Gabor filter function. Thus, Gabor functions can also be used as a band-pass filter.

b) TWO-DIMENSIONAL GABOR FILTER FUNCTION

A general 2-D Gabor filter is a sinusoidal grating which is modulated by a two-dimensional Gaussian function, with the modulation frequency 'W' can be defined as:

$$GB(x, y) = g_\sigma(x, y) exp[2\pi j W(x\cos\theta + y\sin\theta)]$$

where,

$$g_\sigma(x, y) = \frac{1}{2\pi\sigma_x\sigma_y} exp\left[-\frac{1}{2}\left(\frac{x^2}{\sigma_x^2} + \frac{y^2}{\sigma_y^2}\right)\right]$$

The parameter σ represents the scale, θ represents the orientation parameter, and W is the modulation frequency of the Gaussian function. These parameters viz. the scale and local direction are used for tuning and various settings for other textural analysis of the Gabor filter. The convolution of an image $A(x, y)$with a Gabor function $GB(x, y)$gives a Gabor filtered image.

These Gabor functions produces a non-orthogonal set. These Gabor functions can describe any supposed function $F(x, y)$. Such type of expansion delivers a localized frequency and can be very useful in textural analysis and image compression. However, the localized frequency is not appropriate for feature extraction as it demands a fixed width window in spatial domain and consequently, the bandwidth of frequency is constant on the linear scale. To overcome this drawback and to detect various features at few more scales, varying width window is needed rather than fixed width window. This drawback led to implement Gabor Filter Transform (GWT) which is analogous to wavelet decomposition having basic wavelet as a Gabor function.

The Gabor wavelets are restricted by a two-dimensional Gaussian envelope. These are similar to the complex planar wave having various orientation and scale. Aside from these, two Gabor wavelets can be differentiated by the width and wavelength of the Gaussian envelope.

Each Gabor wavelet contains a particular orientation and wavelength. These are convolved with the image for estimating local frequency magnitude of that approximate orientation and wavelength in the image.

The Gabor wavelets are generally considered as an individual group of self-similar functions. Let $g(x, y)$ be the mother Gabor wavelet, then this self-similar filter set is obtained by suitable rotations and dilations of $g(x, y)$. For an image $A(x, y)$of size $(M\ x\ N)$, the corresponding Discrete Gabor Wavelet Transform (DGWT) is described as:

$$G_{pq}(x, y) = \sum_{s} \sum_{t} A(x - s, y - t).\psi^{*}_{pq}(s, t)$$

where s, t are the variables for size variation of filter mask; q, p are the orientation and the scale values respectively and ψ^{*}_{pq} is complex conjugate of ψ_{pq}, which is the self-similar function produced from the rotation and dilation of the mother wavelet 'ψ' and is defined as

$$\psi(x,y) = \left(\frac{1}{2\pi\sigma_x\sigma_y}\right) exp\left[-\frac{1}{2}\left(\frac{x^2}{\sigma_x^2}+\frac{y^2}{\sigma_y^2}\right)\right] exp(2\pi jWx)$$

The Gabor Wavelet Filters are constructed through the following generating function defined as:

$$\psi(x,y) = a^{-p}\psi(\overline{x},\overline{y})$$

where, $q = 0,1 \ldots Q-1$, and $p = 0,1 \ldots P-1$. Other parameters are the scale factor$a$; the total number of scales is P; total number of orientations is represented by Q.

$$\overline{x} = a^{-p}(x\cos\theta + y\sin\theta)$$

$$\overline{y} = a^{-p}(y\cos\theta - x\sin\theta), \text{ for a} > 1 \text{ and } \theta = \frac{q\pi}{Q}$$

The local frequency magnitude at a particular orientation and scale can be estimated by the convolution of an image and a group of Gabor wavelets. In this study these Gabor Wavelet Filters (GWT) are obtained at 5 different scales and 8 different orientations $(0°, 22.5°, 45°, 67.5°, 90°, 112.5°, 135°, 157.5°)$. A total of 40 GWT are constructed using these settings of orientation and scale. A convolution between these GWT and an image has been done to get 40 Gabor filtered output images. These output images contains different textural information for classification. The energy of each output image is calculated using the following function:

$$EN_{GWT}(p,q) = \sum_x \sum_y G_{pq}(x,y)$$

The standard deviation σ_{GWT} and mean μ_{GWT} of every transformed coefficient are as given below. These values signify the feature of a homogeneous texture image. These features are defined as:

$$\mu_{GWT} = \frac{EN_{GWT}(p,q)}{MN}$$

$$\sigma_{GWT} = \sqrt{\frac{\sum_x \sum_y |G_{pq}(x,y)| - \mu_{pq}}{MN}}$$

3.4.5 LAW'S TEXTURAL ENERGY FEATURES (LTEM)

Apart from above textural classification techniques, Law's Textural Energy (LTEM) is another widely known technique. It was developed by K. I. Laws [37] in 1980. LTEM has various local masks with different length for various textural detection as ripple, wave, spot, edge and level. These local masks are convolved with each other to get different types of convolution masks which computes the energy of the texture of an image.

There are the five types of local masks of length 5, which are defined as:

$$L5 = [+1 \quad +4 \quad 6 \quad +4 \quad +1] \quad (Level)$$

$$E5 = [-1 \quad -2 \quad 0 \quad +2 \quad +1] \quad (Edge)$$

$$S5 = [-1 \quad 0 \quad 2 \quad 0 \quad -1] \quad (Spot)$$

$$W5 = [-1 \quad +2 \quad 0 \quad -2 \quad +1] \quad (Wave)$$

$$R5 = [+1 \quad -4 \quad 6 \quad -4 \quad +1] \quad (Ripple)$$

These five types of local masks are used for different purposes such as

a) Level detection- It calculates the average gray level

b) Edge detection- It calculates the minor and major edges

c) Spot detection- It computes the spots in the texture of an image

d) Wave detection- It also computes the uneven nature of the texture; named as wave detection.

e) Ripple detection- It also analyse the ripples present in the texture.

A total of $(5 \times 5 = 25)$, 2D special convolution masks or filters can be acquired after performing the outer vector product of these 1-D kernels with each other or with themselves. These special filters are as:

$L5L5$	$E5L5$	$S5L5$	$W5L5$	$R5L5$
$L5E5$	$E5E5$	$E5S5$	$S5W5$	$R5E5$
$L5S5$	$E5S5$	$S5S5$	$S5W5$	$S5R5$
$L5W5$	$E5W5$	$S5W5$	$W5W5$	$R5W5$
$L5R5$	$E5R5$	$S5R5$	$W5R5$	$R5R5$

These 25-2D law's masks are then convolved with the ROI of size $M \times N$ selected and generates 25 filtered texture images (TIs).

Another 1D local masks of length 7 are generated from these vectors:

$$L7 = [+1 \quad +6 \quad +15 \quad 20 \quad +15 \quad +6 \quad +1] \quad (Level)$$

$$E7 = [-1 \quad -4 \quad -5 \quad 0 \quad +5 \quad +4 \quad +1] \quad (Edge)$$

$$S7 = [-1 \quad -2 \quad 1 \quad 4 \quad 1 \quad -2 \quad -1] \quad (Spot)$$

These local masks are also used for different purposes such as level-detection, edge-detection, spot-detection on ROI's. $(3 \times 3 = 9)$, 2D special filters are obtained after performing the outer vector product of these 1D kernels with each other or with themselves. These special filters are:

$L7L7$	$E7L7$	$S7L7$
$L7E7$	$E7E7$	$E7S7$
$L7S7$	$E7S7$	$S7S7$

These 9-2D law's masks are then convolved with the ROI of size $M \times N$ selected and generates 9 filtered texture images (TIs). Some of local filters of length 9 are as following:

$$L9 = [1 \quad 8 \quad 28 \quad 56 \quad 70 \quad 56 \quad 28 \quad 8 \quad 1](Level)$$

$$E9 = [1\ \ 4\ \ 4\ \ -4\ \ -10\ \ \ -4\ \ 4\ \ 4\ \ 1](Edge)$$

$$S9 = [-1\ \ \ 0\ \ -4\ \ 0\ \ 6\ \ \ 0\ \ \ -4\ \ \ 0\ \ 1](Spot)$$

$$W9 = [-1\ \ -4\ \ 4\ \ 4\ \ -10\ \ 4\ \ 4\ \ -4\ 1](Wave)$$

$$R9 = [+1\ \ -8\ \ 28\ \ -56\ \ 70\ \ -56\ \ 28\ \ -8\ \ 1]\quad (Ripple)$$

These local masks are used for different purposes such as level detection, edge detection, spot detection, wave detection, ripple detection on ROI's. $(5 \times 5 = 25)$, 2D special filters are attained after performing the outer vector product of these 1-D kernels with each other or with themselves. These special filters are:

$L9L9$	$E9L9$	$S9L9$	$W9L9$	$R9L9$
$L9E9$	$E9E9$	$E9S9$	$S9W9$	$R9E9$
$L9S9$	$E9S9$	$S9S9$	$S9W9$	$S9R9$
$L9W9$	$E9W9$	$S9W9$	$W9W9$	$R9W9$
$L9R9$	$E9R9$	$S9R9$	$W9R9$	$R9R9$

3.5 ARTIFICAL NEURAL NETWORK (ANN) CLASSIFIER

It is a technique which is used for classification of input prototypes into equivalent analogous classes. There are many factors which affects the selection process of a classifier, those factors are: algorithm performance, classification accuracy and computation resources.

A conventional Artificial Neural Network (ANN) is a mathematical system which has non-linear artificial neurons. An ANN can be multi-layered ANN or single-layered ANN. Multi-layered ANN mostly has three layers: input, hidden, and output layer. The feature vector is given as an input to the input layer. The input layer has equal number of neurons as the number of features extracted i.e. feature vector length. An output layer with three neurons has selected as three brain tumor classes has to be classified. Every output layer neuron gives a '1' according to the label class defined for it and gives a '0' for another output neurons. The hidden layer neurons communicate between the output layer neurons and the external input layer neurons. A guess and check method is used to find the appropriate number of neurons

for hidden layer. It was concluded after a number of trials that 18 number of neurons are suitable for classification and also for a fast convergence. The leave-one-out cross-validation is not used. The most intense computations take place in the training period. Once these computations are done, the testing and validation process will become relatively fast.

One of the main building blocks of ANN is the ability to *learn*. It is not only one of the complex systems, but also a complex adaptive system i.e. this system is able to vary its internal structure and parameters based on the data which is flowing through it.

A supervised learning is opted for this ANN classifier with back-propagation weight adjustment. Generally, there are two types of signal in this classifier. First is input signal which acts at the classifier input neurons. This input signal propagates forward towards hidden neuron layer and then finally reaches at the output neuron layer, then it is called output signal. Second signal is error signal which starts at the output layer and goes backward (layer by layer).

The output of the ANN is:

$$O = A_o\left(\sum_{m=0}^{J} W_{0m}\left(A_h\left(\sum_{n=0}^{I} W_{mn}\,X_n\right)\right)\right)$$

where, W_{0m} signifies synaptic weights of hidden layer to a single output layer neuron, A_h and A_o signifies the activation function of hidden layer neurons respectively and output layer neurons, X_n is the nth input vector element, W_{mn} is the hidden layer and input layer connection weights.

Fig. 3.10 ANN classifier structure

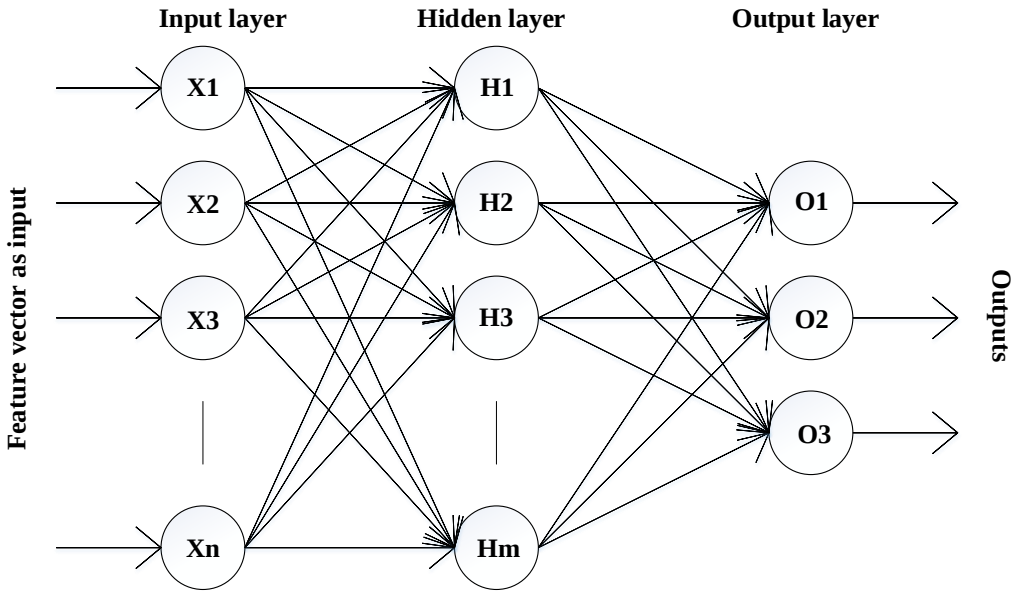

3.5.1 ACTIVATION FUNCTION

An ANN has various processing elements with a single output and a synaptic input connection. The input neuron's signal flow X_i is unidirectional [38]. The relationship between the signals of output neuron is described as:

$$Output\left(O_j\right) = f(\varphi)$$

a) LINEAR ACTIVATION FUNCTION

It can generate only positive values over the full real number range.

$$span: -\infty < O < \infty$$

$$O = X \times S$$

$$D = 1 \times S$$

where, O is output, X is the input, S is the steepness, and D is the derivation of O with respect to X. It can not be efficient in fixed point.

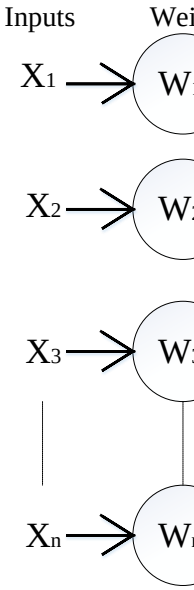

Fig. 3.11 Activation function structure of ANN classifier

b) SIGMOIDAL ACTIVATION FUNCTION

It has positive values between 0 and 1. It is very much efficient with the training data between 0 and 1. This signal is one of the mostly used activation functions.

$$span: 0 < O < 1$$

$$O = \frac{1}{(1 + \exp(-2.S.X))}$$

$$D = 2 \times S \times O \times (1 - O)$$

c) SIGMOIDAL STEPWISE ACTIVATION FUNCTION

It is the piecewise linear approximation of the conventional sigmoidal function. It also has a output between 1 and 0 with an advantage of higher calculation speed than the sigmoid but it is less precise.

d) SIGMOIDAL SYMMETRIC ACTIVATION FUNCTION

It has output values between -1 and 1 with a general tanh function. This activation function is also used frequently.

$$span: -1 < O < 1$$

$$O = \frac{2}{(1 + \exp(-2 * S * X)) - 1}$$

$$D = S \times (1 - (O \times O))$$

e) SIGMOIDAL SYMMETRIC STEPWISE ACTIVATION FUNCTION

This signal is the linear piecewise approximation of the conventional sigmiod function. The output lies between -1 and 1 with higher computational speed than the sigmoidal symmetric activation function.

f) GAUSSIAN ACTIVATION FUNCTION

The Gaussian function is veru efficient where a precise control is needed ranther than the activation function range. The output values lies within 0 to 1. It provides a 0 output value when $X = \infty$ and 1 when $X = 0$.

$$span: 0 < O < 1$$

$$O = \exp(-X * S * X * S)$$

$$D = -2 * X * S * O * S$$

g) GAUSSIAN SYMMETRIC ACTIVATION FUNCTION

This function is the piecewise linear approximation of the above function. It is preferred for the finer controlling ability.

$$span: -1 < O < 1$$

$$O = \exp(-X * S * X * S) * 2 - 1$$

$$D = -2 * X * S * (O + 1) * S$$

h) ELLIOT ACTIVATION FUNCTION

It is the approximate replica of the Hyperbolic Tangent Activation Function (HTF) with much higher speed.

$$span: 0 < O < 1$$

$$O = \frac{\big((X * S)/2\big)}{(1 + |X * S|)} + 0.5$$

$$D = \frac{(S * 1)}{(2 * (1 + |X * S|) * (1 + |X * S|))}$$

i) ELLIOT SYMMETRIC ACTIVATION FUNCTION

This is the higher speed version of the Elliot Activation Function.

$$span: -1 < O < 1$$

$$O = \frac{\big((X * S)\big)}{(1 + |X * S|)} + 0.5$$

$$D = \frac{(S * 1)}{((1 + |X * S|) * (1 + |X * S|))}$$

j) LINEAR PIECEWISE ACTIVATION FUNCTION

Linear piecewise activation function is also known as saturating linear function. It may have bipolar or binary range.

$$span: 0 < O < 1$$

$$O = X * S$$

$$D = 1 * S$$

k) LINEAR PIECE SYMMETRIC ACTIVATION FUNCTION

$$span: -1 < O < 1$$

$$O = X * S$$

$$D = 1 * S$$

CHAPTER 4

RESULTS AND DISCUSSIONS

4.1 EXPERIMENTAL SET UP

The Experiments performed are divided in two segments to test the performance and robustness of additional features approach over less features approach with ANN.

Experiment 1: Initially in this experiment, three tumor classes are classified using ANN approach without LTEM features. Training, validation and testing are the three stage used for

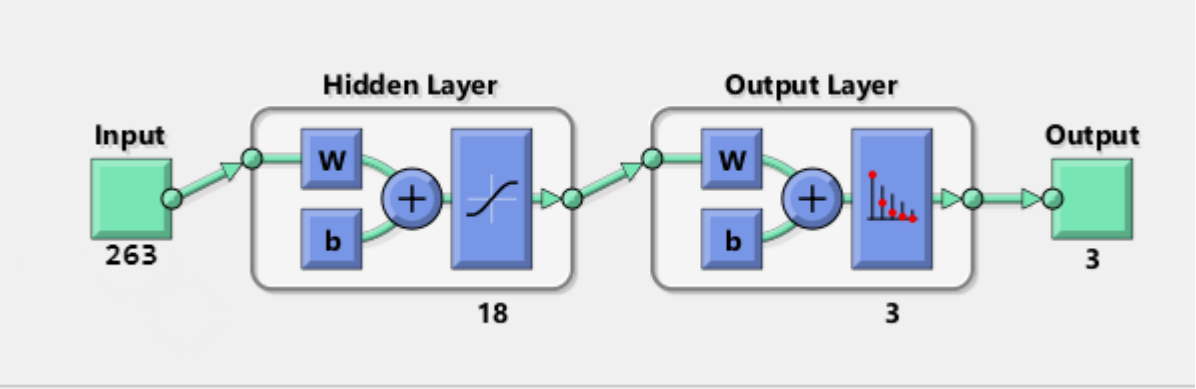

Fig. 4.1 The Structure of ANN Classifier without LTEM's Features

multi-layer ANN classifier. Depending upon the stages of multi-layer ANN classifier, three sets of database has been built namely: training set, validation set, and testing set. Training set has 30% ROI (s) from each class. Validation set has 10% of ROI (s) from each class. As the validation process is completed, ANN optimizes its parameter and performs independent evaluation consisting of 60% of ROI(s) as a testing set. The dataset used for training is not repeated in testing i.e. random selection method has not been applied.

Experiment 2: In the second experiment also, the dataset used for training is not repeated in

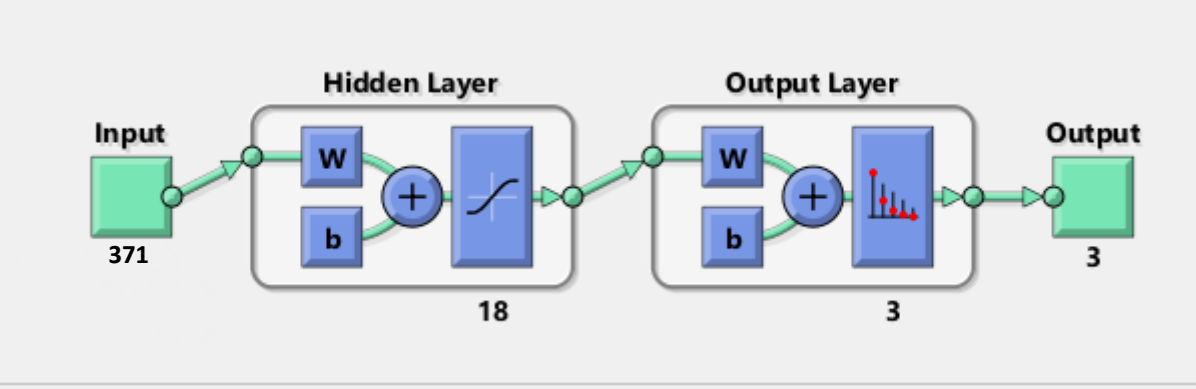

Fig. 4.2 The Structure of ANN Classifier with LTEM's Features

testing i.e. random selection method has not been applied. A selection of 30% ROIs has been made for the training set from each class. The validation set has 10% ROIs from each class. As the validation process is completed, ANN sets all its parameters optimally fixed. Now, ANN is ready for independent evaluation of the test set which consists 60% ROIs. In this experiment, an analysis has been performed on the effect of LTEM features in classification of these ROIs with ANN classifier. The basic data structure used for evaluation is Confusion Matrix. Confusion matrix is the basic parameter for performance calculation of the developed CAD system.

4.1.1 DATASET

The database used is of post-contrast T1 weighted MR images. These images are provided by Surgical Planning Laboratory, Departments of Radiology, Brigham and Women's Hospital, Harvard Medical School, Boston, MA, USA [39, 40]. This database contains brain MR-images of Astrocytoma, Meningioma, and Glioma. All images are obtained using the same MRI equipment (Siemens Verio, Erlangen Germany, and 3 Tesla MR Scanner). From this database, 105 images of MENI (Class-1) & AST (Class-2) are taken. Gliomas are rejected due to the high salt and pepper noise on the images. The Normal regions (NORM-Class 3) are marked from these 105 images to have variant data of white matter and gray matter. T1 images are especially used to distinguish gray and white matter where gray matter is dark gray (iso to hypo), white matter is light gray (hyper). The normal region gets disarticulated due to spreading of the tumor and leakage of cerebrospinal fluid (CSF). The regions near to tumor are marked specifically as the ad-joint normal area shows a bit similar properties to that of tumor. Therefore, radiologists and neurosurgeons find it difficult to locate the exact boundary of tumor. Therefore, ROI(s) of the normal region are considered in this work. The tumor boundaries of MENI (Class-1), AST (Class-2) and NORM (Class-3) ROIs are marked by the expert radiologist in the present work and are taken as ground truth.

4.1.2 SOFTWARE

This method is implemented in MATLAB 2015a and MR images of size 256×256 is taken for testing. This method is performed on notebook PC HP ENVY having 8 GB RAM with Intel(R) Core (TM) i5-4200 CPU@ 2.50 GHz.

4.1.3 ROI SIZE

ROI's of size 20×20 is segregated from the database. A total of 105 ROIs are segregated from the database where each class has 35 ROIs. Specific size of ROI i.e. 20×20

are taken as the secondary database for the feature extraction (explained in detailed in chapter 3 section 3.3 on page no 19).

4.1.4 FEATURES EXTRACTED

From these ROI(s) 371 number of features are extracted. These features depend upon the texture, intensity of the image.

Table 4.1 An overview of total features

S.NO.	FEATURE NAME	FEATURE TYPE AND ORIENTATION	NUMBER OF FEATURES
1.	FOS	Intensity based feature	11
2.	GLCM	Texture based feature at $0°, 45°, 90°, 135°$ with offset value '1'	$22 \times 4 = 88$
3.	GLRLM	Texture based feature at $0°, 45°, 90°, 135°$	$11 \times 4 = 44$
4.	GABOR WAVELETS	Texture based feature at 8 different angles $(0°, 22.5°, 45°, 67.5°, 90°, 112.5°, 135°, 157.5°)$ with 5 scales. From these convolved images mean, entropy, and energy are calculated.	$8 \times 5 \times 3 = 120$
5.	LAW'S TEXTURAL ENERGY FEATURES	Texture based features with 5, 7, 9 length filters. From convolved images mean, entropy, and energy are calculated.	$(15 + 6 + 15) \times 3 = 108$
	TOTAL FEATURES		**371**

The results of the LTEM feature extraction technique are:

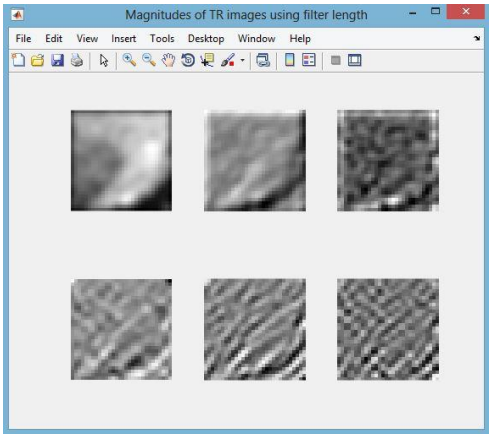

(a)

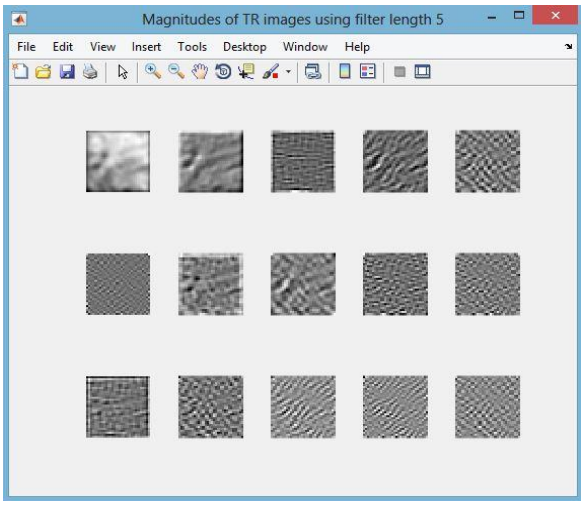

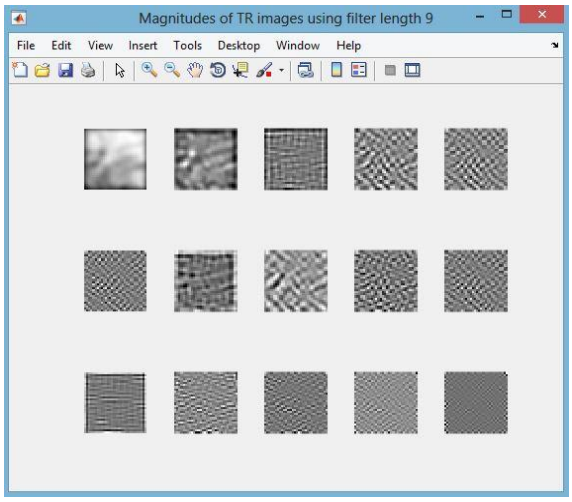

(b) **(c)**

Fig. 4.3 The results of LTEM features **(a)**LTEM filter length 7 results **(b)** LTEM filter length 5 results **(c)** LTEM filter length 9 results

The results of GWT are as following:

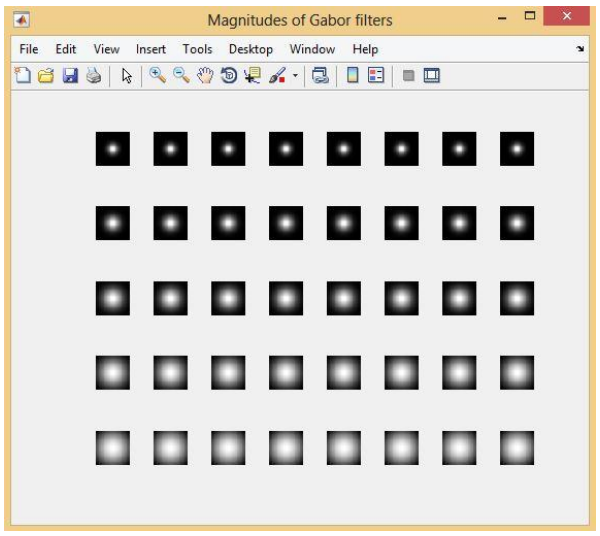

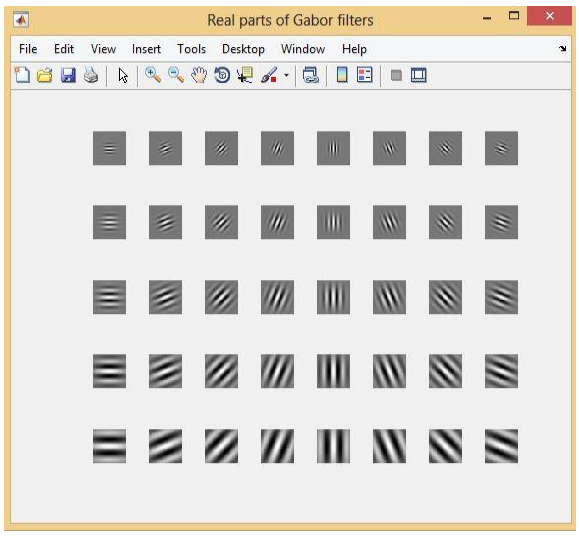

Fig. 4.4 GWT filters with different orientations and scales **(a)** Magnitudes of GWT filter **(b)** Real part of GWT filters

4.1.5 CLASSIFIER

Artificial neural network has been adopted for classification purpose. It is having three major layers namely; input layer, hidden layer, and output layer. Input layer has 371 number of neurons which is equal to number of features extracted. The hidden layer has 18 neurons. These have been taken after trial and error process. Several number of neurons were applied and it was found that 18 neurons are reasonable for this classification purpose. Output layer has three neurons for three classes. .

Leave out one cross validation is not used as it is specific to its use in regression. While predicting quantitative variables (such as individual learning rates) from MRI data, one thing that always has been done when running any predictive analysis is to perform a randomization test to determine the distribution of performance when the relation between the data and the outcome is broken (e.g., by randomly shuffling the outcomes). In a regression analysis, what one expects to see in this randomized-label case is a zero correlation between the predicted and actual values.

The dataset is divided into training, validation, and testing sets. Training set has 30% of the total images. Validation set has 10% of the total images. Testing set 60% of the total images.

4.1.5.1 EVALUATION METRIC

The basic data structure used for evaluation is Confusion Matrix. Confusion matrix is the basic parameter for performance calculation of the developed CAD system. The confusion matrix is based on following parameters:

a) True positive (TP) = Correctly identified in same class as positive cases
b) False positive (FP) = Incorrectly identified in other class as negative cases
c) True negative (TN) = Negative cases classified in same class correctly
d) False negative (FN) = Incorrectly classified in other classes as positive cases

The performance of the ANN is also analysed in terms of the individual class accuracy and overall classification accuracy.These parameters can be described as:

a) Individual class accuracy for a^{th} class $= \left({}^{TP(a)}\!/_{Class(a)} \right)$

b) Overall classification accuracy $= \left({}^{\sum_i TP(a)}\!/_{\sum_i Class(a)} \right) \times 100$

where, class(a) is the number of instances in the secondary database

4.2 RESULTS AND DISCUSSIONS

EXPERIMENT 1:

Initially, in this experiment, three tumor classes are classified using ANN approach without LTEM features. A feature bank consisting FOS, GLCM, GLRLM, and GWT features (a total of 263 features) is taken as an input to the multi-layer ANN classifier. Three different classes viz. MENI (Class-1), AST (Class-2), and NORM (Class-3) are classified. Individual class accuracy for MENI (class-1) is 77.14%, 74.30% for AST (class-2), and 82.86 % for NORM (class-3). An overall classification accuracy of 78.10% is being observed as given in Table 4.2. It is being observed from Table 4.2 that the MENI (Class-1) is highly misclassified with AST (Class-2) and vice-versa. NORM (Class-3) is also misclassified with AST (Class-2) and MENI (Class-1) with lower misclassification rate. MENI (Class-1) is 20% misclassified with AST (Class-2). The higher misclassification between these two classes is due to the hypo as well as hyper intense nature of AST (Class-2) and the cystic and necrotic components in the ROIs.

Table 4.2 Confusion Matrix of Experiment 1

Classes	**Experiment 2 results of ANN classifier with LTEM**		
	MENI (Class-1)	**AST (Class-2)**	**NORM (Class-3)**
MENI (Class-1)	27	6	2
AST (Class-2)	7	26	4
NORM (Class-3)	1	3	29
Individual classification accuracy	**77.14%**	**74.30%**	**82.86%**
Overall classification accuracy	**78.10%**		

EXPERIMENT 2:

An accuracy of 77.14% for MENI (Class-1), 74.30% for AST (Class-2), and 81.81% for NORM (Class-3) has already been delivered in previous experiment. An addition of LTEM features has been done in the feature bank with FOS, GLCM, GLRLM, and GWT features (a total of 371 features). These features are taken as input to the multi-layer ANN classifier. An

overall classification accuracy of 91.43% is being observed as shown in Table 4.3. Individual class accuracy for each class is 91.40% for MENI, 91.43% for AST, and 94.29% for NORM. Training set has 30% ROI (s) from each class. Validation set has 10% ROI (s) from each class. As the validation process is completed, ANN sets all its parameters optimally fixed. Now, ANN is ready for independent evaluation of the test set which consists 60% ROI (s). It is observed from Table 4.3 that the misclassification between MENI (Class-1) and AST (Class-2) has been reduced. An improvement of 12% has been observed from the Table 4.3, as initially the misclassified between MENI (Class-1) and AST (Class-2) is 20% but after addition of LTEM features the misclassification between these two classes is reduced to 8%. This improvement in classification has been achieved with the help of LTEM features as it has the capability to detect fundamental texture patterns viz. level, spot, wave, ripple, and edge. It is also been observed that the LTEM features can clearly differentiate MENI (Class-1) and AST (Class-2) despite of necrotic and cystic components, location and size of the tumors. More than 30% ROI in training stage can further improve the individual classification accuracy as well as overall classification accuracy.

Classes	**Experiment 2 results of ANN classifier with LTEM**		
	MENI (Class-1)	**AST (Class-2)**	**NORM (Class-3)**
MENI (Class-1)	32	2	1
AST (Class-2)	3	32	1
NORM (Class-3)	1	1	33
Individual classification accuracy	**91.40%**	**91.43%**	**94.29%**
Overall classification accuracy	**92.43%**		

Table 4.3 Confusion Matrix of Experiment 2

CHAPTER 5

CONCLUSION

An adequate computer aided diagnosis (CAD) system has been developed with additional features and improved accuracy for classification of brain tumors. The performance of this CAD system has been analysed through ANN classifier with a multifarious database of real post contrast T1-weighted MR-images. This database consisted of 20×20 size ROIs of primary brain tumors namely MENI (class 1), AST (class 2) and NORM (class 3). Total 371 texture and intensity features are extracted from these ROIs. Artificial neural network (ANN) has been used to classify these three classes as it provided better results with individual class accuracy and overall classification accuracy. The two discrete experiments have been performed. In the first experiment 263 features are extracted and an overall classification accuracy 78.10% is achieved, however it was noticed that MENI (class 1) was highly misclassified with AST (class 2). In experiment 2, 371 features are taken. The improved individual classification accuracy of 91.40% is obtained for MENI (class 1), 91.43% for AST (class 2), and 94.29% for NORM (class 3) and an overall classification accuracy of 92.43% is achieved. It is noted from Table 4 that misclassification rate is quite low for MENI (class 1). This is due to addition of 108 LAW's textural energy measures (LETM). It is observed that the texture patterns obtained by adding LETM provided clear differentiating capability between MENI (class1) and AST (class 2) despite of necrotic and cystic component, location, and size of tumor. This is due to their inherent property of detection of fundamental texture features such as level, edge, spot, wave and ripple in both horizontal and vertical directions which boosted the texture energy. Overall, an improved CAD system by experimentation has been developed for the young and inexperienced radiologists as well as medical students.

CHAPTER 6

FUTURE WORK

There are some additions which can be possibly made in this research work, those are:

a) An increment in the database can be possibly done for an improved classification system with more variety of tumors.
b) An increment in the type of brain tumor classification can be done.

REFERENCES

[1] Wilson, Atkins K, Waugh, Chambers A, Grant G, Ross A, Janet, "Ross and Wilson anatomy and physiology in health and illness", Edinburgh: Churchill Livingstone, pp. 53–54. ISBN 0-443-10101-9, 2006.

[2] Strayer D L, Rubin R, Rubin, Emanuel, "Clinic-pathologic foundations of medicine", Rubin's pathology, Philadelphia: Wolters Kluwer/Lippincott Williams & Wilkins. pp. 138–139. ISBN 0-7817-9516-8, 2008.

[3] "Apparatus and Method for Detecting Cancer in Tissue". United States Patent and Trademark Office.

[4] Arimura H, Magome T, Yamashita Y, Yamamoto D, "Computer-aided diagnosis systems for brain diseases in magnetic resonance images", Algorithms, 2(3), 925–952, 2009.

[5] Cherkassky V, Mulier F, "Learning from data: Concepts, theory and methods (2nd edition)", John Wiley and Sons.

[6] Fujita H, Uchiyama Y, Nakagawa T, Fukuoka D, Hatanaka Y, Hara T, "Computer-aided diagnosis: The emerging of three CAD systems induced by Japanese health care needs", Computer Methods and Programs in Biomedicine, 92(3), 238–248, 2008.

[7] Mohsen H, Dahshan EI, Salem A., "A machine learning technique for MRI brain images", In Proceedings of the (8th) 2012 INFOS IEEE international conference on informatics and systems (INFOS2012), pp. BIO-161 - BIO-165, Print ISBN: 978-1-4673-0828-1

[8] Lev M H, Ozsunar Y, Henson J W, Rasheed A A, Barest G D, Harsh G R, Fitzek M M, Chiocca E A, Rabinov J D, Csavoy A N, Rosen B R, Hochberg F H, Schaefer P W, Gonzalez R G, "Glial Tumor Grading and Outcome Prediction Using Dynamic Spin-Echo MR Susceptibility Mapping Compared with Conventional Contrast-Enhanced MR: Confounding Effect of Elevated rCBV of Oligodendro-glimoas". Am J Neuroradiol.2004; 25:214–221.

[9] Kremer S, Grand S, Remy C, Esteve F, Lefournier V, Pasquier B, Hoffmann D, Benabid AL, Le Bas JF, "Cerebral blood volume mapping by MR imaging in the initial evaluation of brain tumors", Journal of Neuroradiology, 29:105, 2002.

[10] Provenzale J M, Mukundan S, Baroriak D P, "Diffusion-weighted and Perfusion MR Imaging for Brain Tumor Characterization and Assessment of Treatment Response", Radiology; 239:632–649, 2006.

[11] Devos A, Simonetti A W, Graff M V, Lukas L, Suykens J A K, Vanhamme L, Buydens L M C, Heerschap A, Vanhuffel S, "Classification of brain tumors using short time echo H MR spectra" , J. Magn. Reson., vol. 170, pp.164-175, 2004.

[12] Devos A, Lukas L, Suykens J A K, Vanhamme L, Tale A R, Howe F A, Moreno-Torres A, Heerschap A, Vanhuffel S, Graff M V, "The Use of multivariant MR imaging intensities versus metabollic data from MR spectroscopic imaging for brain tumor classification" , J. Magn. Reson., vol. 173, pp.218-228, 2005.

[13] Wang Q, Liacouras E K, Miranda E, Kanamala U S, Megalooikonomou V, "Classification of brain tumors using MRI and MRS". Proceedings of the SPIE Conference on Medical Imaging, 2007.

[14] Zarcharaki E I, Wang S, Chawla S, Yoo D S, Wolf R, Melhem E R, Davatzikos C, "Classification of brain tumor type and grade using MRI texture in a Machine Learning Technique", Magn. Reson. Med., vol.62, pp.1609-1618, 2009.

[15] Georgiardis P, Cavouras D, Kalatzis I, Daskalakis A, Kagadis GC, Malamas M, Nikifordis G, Solomou E, "Improving brain tumor characterization on MRI by probabilistic neural network on non-linear transformation of textural features", Comput Meth Prog bio., vol. 89, pp. 24-32, 2008.

[16] Li H, Giger M L, Huo Z, Olopade O L, Lan L, Weber B I, Bonta I, "Computerized analysis of mammographic patterns for assessing breast cancer risk: Effect of ROI size and location", Medical Physics, vol. 31 no. 3, pp. 549-555, 2004.

[17] Jeon J H, Choi J Y, Lee S and Ro Y M, "Multiple ROI selection based focal liver lesion classification in ultrasound images", Expert Systems with Applications, vol. 40 no. 2, pp. 450-457, 2013.

[18] Kadah Y M, Farag A A, Zurada J M, Badawi A M, Youssef A M, "Classification algorithms for quantitative tissue characterization of diffuse liver disease from ultrasound images", IEEE Transactions on Medical Imaging, vol. 15 no. 4, pp. 466-78, 1996.

[19] Haralick, Shanmugum, R M K, Dinstein I, "Textural Features for Image Classification", IEEE Trans System Man Cybernet, 3:610-621, 1973.

[20] Selvaraj H, Thamarai S S, Selvathi D, Gewali L B, "Brain MRI slices classification using least squares support vector machine", J. Intell. Comput. Med Sciences, 1:21-33, 2009.

[21] Kharrat A, Gasm K, "Hybrid approach for automatic classification of brain MRI using genetic algorithm and support vector machine", Leonardo Journal of Sciences, 17: 71-82, 2010.

[22] Zacharaki E I, Wang S, Chawla S, Yoo D S, Wolf R, Mehem E R, Davatzikos C, "Classification of brain tumor and grade using MRI texture in a Machine Learning technique", Magn. Reson. Med., vol.62 pp. 1609-1618, 2009.

[23] Georgiardis P, Cavouras D, Kalatzis I, Daskalakis A, Kagadis G C, Malamas M, Nikifordis G, Solomou E, "Improving brain tumor characterization on MRI by probabilistic neural network on non-linear transformation of textural features", Comput Meth Prog bio., vol. 89, pp. 24-32, 2008.

[24] Georgiardis P, Cavouras D, Kalatzis I, Daskalakis A, Kagadis G C, Malamas M, Nikifordis G, Solomou E, "Non-linear least square feature transformations for improving the performance of probabilistic neural networks in classifying human brain tumors on MRI", Lecture notes on computer science, 4707:239-247, 2007.

[25] Kumar V, Sachdeva J, Gupta I, Khandelwal N, Ahuja C, "Classification of brain tumors using PCA-ANN", In proceedings, IEEE conference on Information and Communication Technologies (WICT), 2011 World Congress, pp. 1079-1083, Mumbai, DOI:10.1109/WICT.2011.6141398, 2011.

[26] Sachdeva J, Kumar V, Gupta I, Khandelwal N, Ahuja C, "Multiclass Brain Tumor Classification Using GA-SVM", In proceedings, IEEE conference on Developments in E-systems Engineering (DeSE), pp. 182-187, Dubai, Dec 2011. DOI: 10.1109/DeSE.2011.31, 2011.

[27] Shaikhli A L, S D S, Yang M Y, Rosenhahn B, "Brain tumor classification using sparse coding and dictionary learning", Image Processing (ICIP), 2014 IEEE International Conference on DOI: 10.1109/ICIP.2014.7025561, Page(s): 2774 – 2778, 2014.

[28] Kadah Y M, Farag A A, Zurada J M, Badawi A M, Youssef A M, "Classification algorithms for quantitative tissue characterization of diffuse liver disease from ultrasound images", IEEE Transactions on Medical Imaging, vol. 15 no. 4, pp. 466-78, 1996.

[29] Christodoulou C I, Pattichis C S, Pantziaris M, Nicolaides A, "Texture-based classification of atherosclerotic carotid plaques", IEEE Trans Med Imaging 2003; 22(7):902–12, 2003.

[30] Stoitsis J, Valavanis I, Mougiakakou S G, Golemati S, Nikita A, Nikita K S, "Computer-aided diagnosis based on medical image processing and artificial intelligence methods", Nuclear Inst Meth Phys Res 2006; 569: 591–5.

[31] Soh L, Tsatsoulis C, "Texture analysis of SAR sea ice imagery using gray level co-occurrence matrices", IEEE Trans Geosci Remote Sens 1999; 37: 780–95.

[32] Clausi D A, "An analysis of co-occurrence texture statistics as a function of grey level quantization" Can J Remote Sens 2002; 28: 45–62.

[33] Galloway M M, "Texture analysis using gray level run lengths," Comput. Graphics Image Process. , vol. 4, pp. 172–179, June 1975.

[34] Tang X, "Texture information in run-length matrices", IEEE Trans Image Process 1998; 7(11):1602–9.

[35] Gabor D, "Theory of communication", Journal of the Institution of Electrical Engineers – Part III: Radio and Communication Engineering, 93(26):429–457, Nov. 1946.

[36] Manjunath B S, Ma W Y, "Texture features for browsing and retrieval of image data", IEEE Trans Pattern Anal Mach Intell 1996; 18:837–42.

[37] Laws K, "Textured image segmentation," Ph.D. dissertation, University of Southern California, 1980.

[38] Jacek M, Zurada, "Introduction to Artificial Neural Systems", pp 32-36, 2006.

[39] Kaus M, Warfield SK, Nabavi A, Black PM, Jolesz FA, Kikinis R. Automated segmentation of MRI of brain tumors. Radiology 2001; 218(2):586–91. Available online http://www.spl.harvard.edu/publications/item/view/169.

[40] Warfield SK, Kaus M, Nabavi A, Black PM, Jolesz FA, Kikinis R. Adaptive template moderated, spatially varying statistical classification.Med Image Anal 2000;4(1):43–55. Available online http://www.spl.harvard.edu/publications/item/view/209.

FIGURE REFERENCE

[41] http://www.investinlibya.org/ brain-diagram-unlabeled

[42] http://www.abta.org/brain-tumor-information/types-of-tumors/meningioma.html?referrer=https://www.google.co.in/

[43] http://www.catholica.com.au/gc2/dw/004_dw_261208.php